

Pyroelectric properties of Al(In)GaN/GaN hetero- and quantum well structures

O Ambacher¹, J Majewski¹, C Miskys¹, A Link¹, M Hermann¹,
M Eickhoff¹, M Stutzmann¹, F Bernardini², V Fiorentini², V Tilak³,
B Schaff³ and L F Eastman³

¹ Walter Schottky Institute, TU-Munich, Am Coulombwall, D-85748 Garching, Germany

² Istituto Nazionale per la Fisica della Materia, Dipartimento di Fisica, Università degli Studi di Cagliari, Italy

³ Electrical and Computer Engineering, Cornell University, Ithaca, NY 14853-5401, USA

Received 26 September 2001, in final form 7 November 2001

Published 22 March 2002

Online at stacks.iop.org/JPhysCM/14/3399

Abstract

The macroscopic nonlinear pyroelectric polarization of wurtzite $\text{Al}_x\text{Ga}_{1-x}\text{N}$, $\text{In}_x\text{Ga}_{1-x}\text{N}$ and $\text{Al}_x\text{In}_{1-x}\text{N}$ ternary compounds (large spontaneous polarization and piezoelectric coupling) dramatically affects the optical and electrical properties of multilayered Al(In)GaN/GaN hetero-, nanostructures and devices, due to the huge built-in electrostatic fields and bound interface charges caused by gradients in polarization at surfaces and heterointerfaces. Models of polarization-induced effects in GaN-based devices so far have assumed that polarization in ternary nitride alloys can be calculated by a linear interpolation between the limiting values of the binary compounds. We present theoretical and experimental evidence that the macroscopic polarization in nitride alloys is a nonlinear function of strain and composition. We have applied these results to interpret experimental data obtained in a number of InGaN/GaN quantum wells (QWs) as well as AlInN/GaN and AlGaIn/GaN transistor structures. We find that the discrepancies between experiment and *ab initio* theory present so far are almost completely eliminated for the AlGaIn/GaN-based heterostructures when the nonlinearity of polarization is accounted for. The realization of undoped lattice-matched AlInN/GaN heterostructures further allows us to prove the existence of a gradient in spontaneous polarization by the experimental observation of two-dimensional electron gases (2DEGs). The confinement of 2DEGs in InGaIn/GaN QWs in combination with the measured Stark shift of excitonic recombination is used to determine the polarization-induced electric fields in nanostructures. To facilitate inclusion of the predicted nonlinear polarization in future simulations, we give an explicit prescription to calculate polarization-induced electric fields and bound interface charges for arbitrary composition in each of the ternary III–N alloys. In addition, the theoretical and experimental results presented here allow a detailed comparison of the predicted electric fields and bound interface charges with the measured Stark shift and the sheet carrier concentration of polarization-induced 2DEGs. This comparison provides an insight into the reliability of the calculated nonlinear piezoelectric and spontaneous polarization of group III nitride ternary alloys.

1. Introduction

It has been predicted by theory and confirmed by experiment recently that InN, GaN and AlN with wurtzite crystal structure are pyroelectric materials [1–4]. Characteristic for these crystals, especially for AlN, are large values of pyroelectric (spontaneous) polarization up to $|P_{\text{AlN}}^{\text{SP}}| = 0.09 \text{ C m}^{-2}$, which are present without any external electric field. In contrast to ferroelectric crystals, the orientation of this spontaneous polarization is always along the $[000\bar{1}]$ direction and cannot be inverted by external electric fields. The orientation of the spontaneous polarization relative to the c -axis can only be controlled by adjusting the polarity of the material [1, 5, 6].

Although the spontaneous polarization is very strong in group III nitrides, the pyroelectric coefficients, describing the change of the spontaneous polarization with temperature, are measured to be surprisingly small (e.g. $dP_{\text{AlN}}^{\text{SP}}/dT = 7.5 \mu\text{C K}^{-1}\text{m}^{-2}$, at room temperature [4, 7]), which is considered to be a big advantage in using these materials for high-power and high-temperature applications such as surface acoustic wave (SAW) devices, high-frequency, high-power transistors (HEMTs), microwave amplifiers or very bright light emitting diodes (LEDs) and lasers.

Pyroelectric crystals are always piezoelectric. The piezoelectric constants of group III nitrides are a factor of 5–20 larger than those of InAs, GaAs and AlAs [1]. The high piezoelectricity of GaN and AlN in combination with the high stiffness and sound velocity has already been used to process SAW devices for electric filters with transfer frequencies above 1 GHz [8, 9]. In addition, SAW devices have been successfully applied to measure the elastic and piezoelectric constants of GaN and AlN [10, 11].

Using the measured and predicted elastic and piezoelectric constants it has been previously shown that effects induced by spontaneous and piezoelectric polarization can have a substantial influence on the concentration, distribution and recombination of free carriers in strained group III nitride heterostructures. Observations of Franz–Keldysh oscillations and Stark effects in InGaN/GaN and AlGaIn/GaN QW structures provide direct evidence for the presence of strong electric fields caused by gradients in spontaneous and piezoelectric polarization [12–14]. These fields significantly influence the distribution and lifetime of excess carriers in InGaIn and GaN QWs and can have an important impact on the performance of AlGaIn/GaN- and InGaIn/GaN-based optoelectronic devices. Although these devices, for example continuous green LEDs and blue lasers, have already reached outstanding performance such as output powers of 10 and 30 mW, respectively, further improvements of design and efficiency seem to be possible only on the basis of a more detailed understanding of polarization in group III nitride nanostructures [15, 16].

The importance of polarization-induced effects is further emphasized in the case of pseudomorphic, wurtzite AlGaIn/GaN-based transistor structures [6], which have been the subject of intense recent investigation and have emerged as attractive candidates for high-voltage, high-power operation at microwave frequencies [17–23]. Contributing to the outstanding performance of AlGaIn/GaN-based HEMTs is the ability to achieve polarization-induced 2DEGs with sheet carrier concentrations up to $2 \times 10^{13} \text{ cm}^{-2}$, well above those observed in other III–V material systems. These high sheet carrier concentrations enable the fabrication of AlGaIn/GaN-based HEMTs with channel current densities above 1000 mA mm^{-1} , breakdown voltages of 140 V and cut-off frequencies of $f_t = 68 \text{ GHz}$ and $f_{\text{max}} = 140 \text{ GHz}$. High output power densities of about 11 W mm^{-1} together with high maximum power added efficiency of 40% have been measured at a frequency of 10 GHz [24]. To successfully model and further optimize the electronic devices, a precise prediction and control of the sheet carrier concentrations as well as electronic transport properties of the

polarization-induced 2DEGs is required. To meet these requirements, the spontaneous as well as piezoelectric polarization of binary and especially of ternary group III nitrides have to be determined with a high accuracy.

Up to now, the spontaneous polarization and piezoelectric constants of the ternary compounds have been determined by linear interpolation of the physical properties of the relevant binary materials. A detailed comparison of the theoretical predictions achieved by this procedure and the corresponding experimental results have revealed a significant discrepancy. For example the predicted sheet carrier concentration of polarization-induced 2DEGs confined at interfaces of $\text{Al}_{0.3}\text{Ga}_{0.7}\text{N}/\text{GaN}$ HEMT structures is about 20% higher than the experimental data [25]. The polarization-induced electric fields calculated from the measured Stark shift of excitonic recombination in AlGaN/GaN-based QWs are also significantly below the theoretical predictions [14]. The discrepancies between measured and calculated electric fields are even more pronounced if InGaN/GaN QW structures are investigated [12].

In this paper we review the theoretical and experimental results of the elastic and pyroelectric properties of binary nitrides with wurtzite crystal structure. We develop an improved method to calculate the piezoelectric and spontaneous polarization of the binary, and, more important, of the ternary group III nitrides, taking nonlinearities due to alloying and/or high internal strain into account. Polarization-induced interface charges and sheet carrier concentrations of 2DEGs are predicted for pseudomorphic InGaN/GaN, AlGaN/GaN and AlInN/GaN QWs and heterostructures on the basis of the improved theory and compared with experimental results achieved by a combination of elastic recoil detection, high-resolution x-ray diffraction (HRXRD), x-ray standing wave, photoluminescence (PL), C - V profiling and Hall effect measurements.

2. First-principles prediction of structural and pyroelectric properties of group III nitrides

In order to predict the pyroelectric polarization of ternary random alloys, the structural, elastic and polarization properties of wurtzite III-V nitrides are calculated from first principles within density-functional theory using the plane-wave ultrasoft pseudopotential method [26,27]. The pseudopotentials for Ga and In include, respectively, the semicore 3d and 4d valence states. A plane wave basis is used to expand the wavefunctions and a cut-off of 350 eV is found to be sufficient to fully converge all properties of relevance here. For k -space summation a Monkhorst-Pack (888) grid is used for the binaries [2], while a (444) is used in the alloy supercell calculations [37]. Lattice constants and internal parameters are calculated using standard total-energy calculation, converging forces and stress to zero within $0.005 \text{ eV \AA}^{-1}$ and 0.01 kbar respectively. Polarization and related quantities are obtained using the Berry phase approach as in previous works [1, 2, 28, 29]. Since we are mainly interested in the effects on polarization due to internal strain of ternary alloys related to size mismatch of the two alloyed nitrides, it is necessary that our calculations reproduce relative mismatches with the highest possible accuracy. Comparing density functional theory calculations we found that GGA [30] has advantages in comparison to LDA in reproducing the relative mismatch between the binary constituents, besides getting closer to the experimental lattice constants and cell internal parameter.

The microscopic structure of a random alloy is represented by periodic boundary conditions using the special quasi-random structure method [31]. We enforce the periodic boundary conditions needed to predict the macroscopic polarization in the Berry phase approach. As a compromise between computational workload and the description of random structures, a 32-atom $2 \times 2 \times 2$ wurtzite supercell is adopted. It is possible to mimic the

statistical properties of a random wurtzite alloy for a molar fraction $x = 0.5$ by suitably placing the cations on the 16 sites available in the cell. Since other molar fractions cannot be described as easily and also because nonlinear effects are expected to be largest for this concentration, our theoretical approach to random alloys is restricted to $x = 0.5$. The predicted nonlinearities of structural and polarization-related properties of $A_xB_{1-x}N$ alloys are approximated by quadratic equations of the form

$$Y_{ABN}(x) = Y_{AN}x + Y_{BN}(1 - x) + bx(1 - x) \quad (1)$$

where

$$b = 4Y_{ABN}(x = 0.5) - 2(Y_{AN} + Y_{BN}) \quad (2)$$

is the bowing parameter. In order to determine the quality of the theoretical predictions and the approximation of the nonlinearities, the calculated physical properties are compared with experimental results in sections 2 and 8.

3. Lattice constants, average bond lengths and bond angles in ternary group III nitrides

The lattice constants $a(x)$ and $c(x)$ of wurtzite group III nitride alloys $A_xB_{1-x}N$ ($Al_xGa_{1-x}N$, $In_xGa_{1-x}N$ and $Al_xIn_{1-x}N$) are predicted to follow the composition-weighted average between the binary compounds AN and BN (Vegard's law) [2]:

$$\begin{aligned} a_{AlGaN}(x) &= (3.1986 - 0.0891x) \text{ \AA} & c_{AlGaN}(x) &= (5.2262 - 0.2323x) \text{ \AA} \\ a_{InGaN}(x) &= (3.1986 + 0.3862x) \text{ \AA} & c_{InGaN}(x) &= (5.2262 + 0.574x) \text{ \AA} \\ a_{AlInN}(x) &= (3.5848 - 0.4753x) \text{ \AA} & c_{AlInN}(x) &= (5.8002 - 0.8063x) \text{ \AA}. \end{aligned} \quad (3)$$

By a combination of HRXRD, Rutherford and elastic recoil detection analysis, Vegard's law can be confirmed for the ternary group III nitrides [32–34]. The agreement between the predicted lattice constants and linear fits of the experimental data

$$\begin{aligned} a_{AlGaN}(x) &= ((3.189 \pm 0.002) - (0.086 \pm 0.004)x) \text{ \AA} \\ a_{InGaN}(x) &= ((3.192 \pm 0.001) + (0.351 \pm 0.004)x) \text{ \AA} \\ a_{AlInN}(x) &= ((3.560 \pm 0.019) - (0.449 \pm 0.019)x) \text{ \AA} \\ c_{AlGaN}(x) &= ((5.188 \pm 0.003) - (0.208 \pm 0.005)x) \text{ \AA} \\ c_{InGaN}(x) &= ((5.195 \pm 0.002) + (0.512 \pm 0.006)x) \text{ \AA} \\ c_{AlInN}(x) &= ((5.713 \pm 0.014) - (0.745 \pm 0.024)x) \text{ \AA} \end{aligned} \quad (4)$$

is better than 2% over the whole range of possible compositions (figures 1(a), (b)).

In contrast to the lattice constants the nearest-neighbour bond lengths, $A-N(x)$ and $B-N(x)$, change only slightly and in a nonlinear way (especially for In containing alloys) as a function of alloy composition, resembling more their values in the binary constituents rather than an average value corresponding to the virtual crystal limit (see figures 2(a), (b) [35–37]). The wurtzite structure of interest here has two types of first-neighbour metal–nitrogen bond distances: $M-N_c$ along the c -axis (one bond) and $M-N_b$ in the basal plane (three bonds),

$$M - N_{c1} = uc \quad (5)$$

$$M - N_{b1} = \sqrt{\frac{1}{3}a^2 + \left(\frac{1}{2} - u\right)^2 c^2} \quad (6)$$

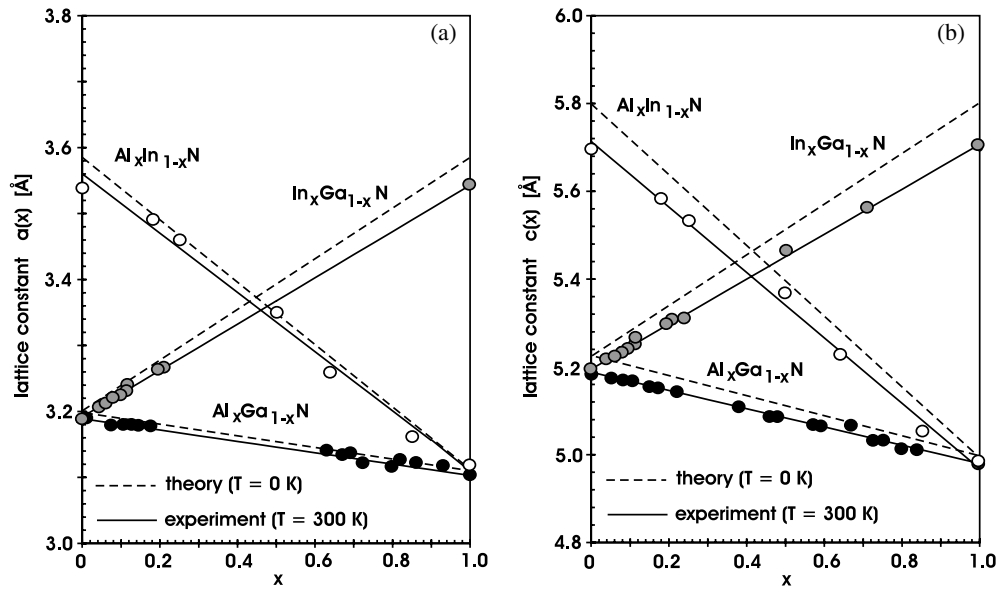


Figure 1. (a) Lattice constant $a(x)$ and (b) lattice constant $c(x)$ for random ternary alloys of group III nitrides measured by HRXRD at room temperature (solid line) and calculated by the method described in section 2 for $T = 0$ K (dashed line). The measured and calculated data confirm the validity of Vegard's law for wurtzite AlGaN, InGaN and AlInN alloys. The agreement between predicted and measured lattice constants is better than 2% over the whole range of possible compositions [31, 33–35].

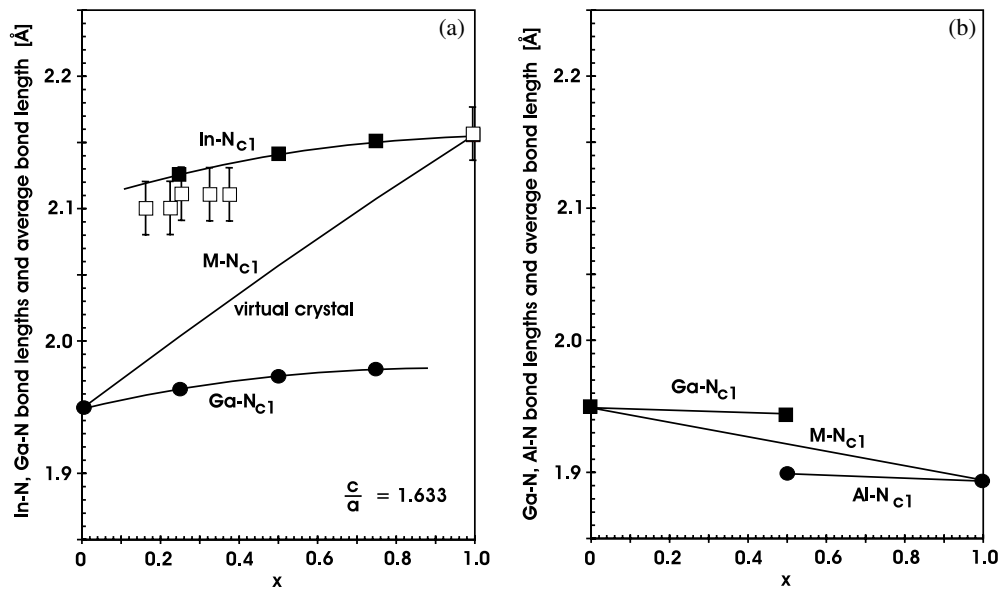


Figure 2. Calculated (black symbols) and measured In-N, Al-N and Ga-N bond lengths (open symbols) for relaxed, random (a) InGaN and (b) AlGaN alloys versus alloy composition [35–37]. The bond length along the c -axis is predicted, assuming a constant c/a -ratio of 1.633. In addition the average bond length $M-N$ of wurtzite (a) InGaN and (b) AlGaN alloys is shown.

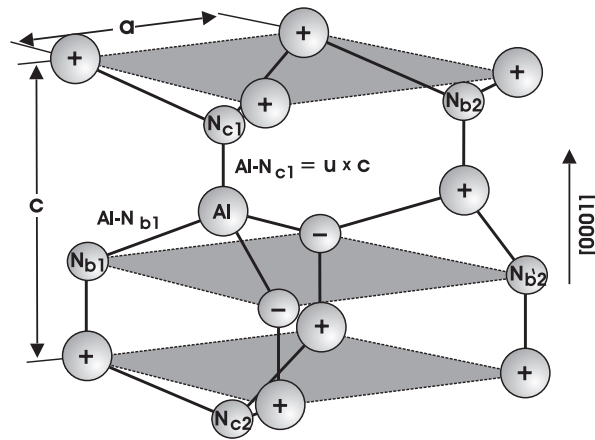


Figure 3. Schematic drawing of a wurtzite AlN crystal with lattice constants a and c . The signs of the charge of metal and nitrogen atoms are indicated as well as the positions of the nearest and second-nearest neighbours to the Al central atom.

and two bond angles $\alpha = \angle (M-N_{c1}; M-N_{b1})$, $\beta = \angle (M-N_{b1}; M-N_{b'1})$ (see figure 5(b)):

$$\alpha = \frac{\pi}{2} + \arccos \left\{ \left(\sqrt{1 + 3 \left(\frac{c}{a} \right)^2 \left(\frac{1}{2} - u \right)^2} \right)^{-1} \right\} \quad (7)$$

$$\beta = 2 \arcsin \left\{ \left(\sqrt{\frac{4}{3} + 4 \left(\frac{c}{a} \right)^2 \left(\frac{1}{2} - u \right)^2} \right)^{-1} \right\}$$

where u denotes the cell internal parameter. In addition three types of second-neighbour cation–anion distance connecting the cation M to the anions N_{c2} , N_{b2} and $N_{b'2}$ (see figure 3) are present:

$$M - N_{c2} = (1 - u)c \quad (\text{one neighbour along the } c\text{-axis}) \quad (8)$$

$$M - N_{b2} = \sqrt{a^2 + (uc)^2} \quad (\text{six neighbours}) \quad (9)$$

$$M - N_{b'2} = \sqrt{\frac{4}{3}a^2 + \left(\frac{1}{2} - u \right)^2 c^2} \quad (\text{three neighbours}). \quad (10)$$

It should be noticed that in the case of an ideal ratio of lattice constants $\frac{c}{a} = \sqrt{\frac{8}{3}} = 1.633$ and ideal cell internal parameter $u = \frac{8}{3} = 0.375$ it follows from equations (5)–(10) that the bond length and the bond angles between the nearest neighbours ($\alpha = \beta = 109.47^\circ$, table 1) are equal, but the distance to the second-nearest neighbour along the c -axis is about 13% shorter than the distance to the other second-nearest neighbours (this is not the case in the cubic structure [36]).

It is known from experiment, as well as theoretical predictions, that neither the cell internal parameter u , nor the c/a -ratio, is ideal in binary group III nitrides (see figures 4(a), (b)) [2,32–34]. In order to evaluate the consequences of the nonideality of the wurtzite structure on polarization and polarization-induced effects in group III nitrides we have calculated the average bond lengths and angles as well as the second-neighbour distances (virtual crystal limit) of ternary alloys taking advantage of the measured and calculated lattice constants and average u parameter. The average cell internal parameter is defined as the average value of the

Table 1. Calculated cell internal parameters, lattice constants and cation–anion distances between nearest and second-nearest neighbours (given in Å) as well as bond angles (given in degrees) of binary, wurtzite group III nitrides with ideal crystal structure or the predicted ‘real’ structure.

	InN		GaN		AlN	
	Ideal	Real	Ideal	Real	Ideal	Real
u	0.375	0.379	0.375	0.377	0.375	0.382
a	3.585	3.585	3.199	3.199	3.110	3.110
c/a	1.633	1.618	1.633	1.634	1.633	1.606
M–N _{c1}	2.195	2.200	1.959	1.971	1.904	1.907
M–N _{b1}	2.195	2.185	1.959	1.955	1.904	1.890
M–N _{c2}	3.659	3.600	3.265	3.255	3.174	3.087
M–N _{b2}	4.204	4.206	3.751	3.757	3.646	3.648
M–N _{b'2}	4.204	4.198	3.751	3.749	3.646	3.639
α	109.47	108.69	109.47	109.17	109.47	108.19
β	109.47	110.24	109.47	109.78	109.47	110.73

projection of the connecting vector pointing from a nitrogen to its nearest-neighbour metal atom in the [0001] direction (figure 3). The u parameter has been calculated for randomly distributed $A_{0.5}B_{0.5}N$ alloys by the theoretical approach described above (more detailed information can be found in [38]) and can be approximated by the following quadratic equations:

$$u_{ABN}(x) = u_{AN}x + u_{BN}(1 - x) + bx(1 - x) \quad (11)$$

$$u_{AlGaN}(x) = 0.3819x + 0.3772(1 - x) - 0.0032x(1 - x)$$

$$u_{InGaN}(x) = 0.3793x + 0.3772(1 - x) - 0.0057x(1 - x) \quad (12)$$

$$u_{AlInN}(x) = 0.3819x + 0.3793(1 - x) - 0.0086x(1 - x).$$

The cell internal parameter is increasing from GaN to InN and, more significantly, to AlN. The nonlinear dependence on alloy composition is described by a negative bowing parameter whose value increases from AlGaN to InGaN and AlInN. It should be pointed out, that although the bowing parameters are negative, the average cell internal parameter of random alloys is always above the ideal value ($u_{ABN} > u_{ideal} = 0.375$). If the lattice constants scale linearly with the alloy composition but the internal parameter does not, the bond angles and/or the bond lengths of the real and the virtual crystal must depend nonlinearly on the alloy composition. The average bond lengths, angles and second-nearest-neighbour distances calculated by using equations (5)–(10) are shown in figures 5(a)–(c) and listed in tables 1 and 2. The average cation–anion distances to the nearest and second-nearest neighbours scale nearly linearly with alloy composition for AlGaN, InGaN and AlInN. The average bond length along the c -axis is 0.7–0.9% longer than the nearest-neighbour bonds in the direction of the basal plane (figure 5(a)). This difference becomes smaller for In containing alloys. The ratio r of the distances to the second-nearest neighbours along the c -axis (M–N_{c2}) and along the basal plane (M–N_{b2}, M–N_{b'2} (figure 5(c))) is well above the ratio of the ideal structure ($r = \{1 - (M-N_{c2}/M-N_{b2})\} = 13\%$) and increases nonlinearly from GaN to InN, reaching 15.4% for AlN (figure 5(d)). The difference between the ideal bond angle $\alpha_{ideal} = 109.47^\circ$ and the average bond angles α and β also increases nonlinearly from GaN to InN and AlN, reaching values of $\Delta\beta = \Delta\alpha = 1.25^\circ$ (figure 5(b)). Besides the significant deviation of the group III nitrides from the ideal wurtzite structure it should be noticed that the observed nonlinearities in the cell internal parameter, cation–anion distances and bond lengths of the random alloys always tend to decrease the difference between the ‘real’ and ideal structure.

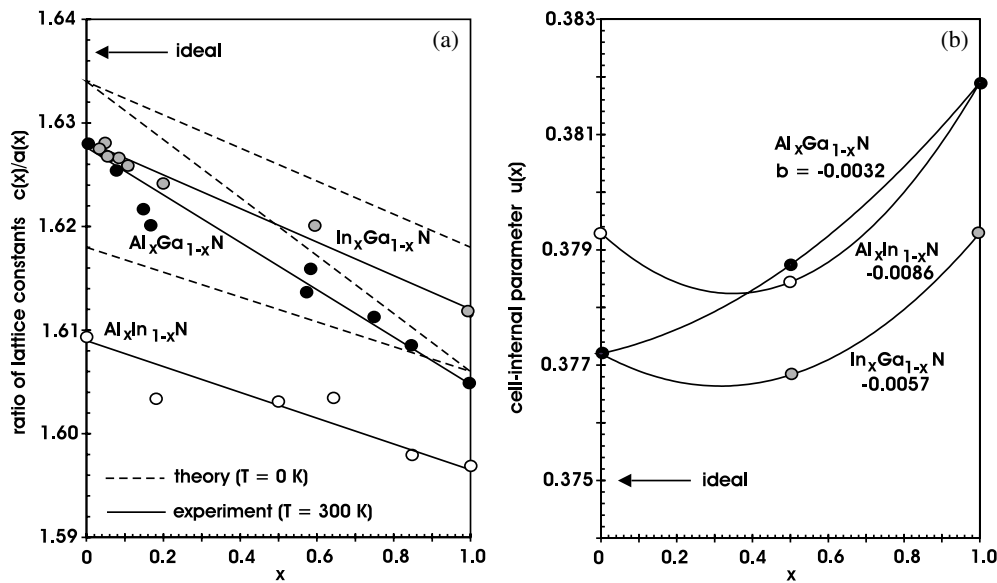


Figure 4. (a) c/a -ratio of random, ternary alloys of group III nitrides measured by HRXRD at room temperature (solid lines) and calculated by the method described in section 2 for $T = 0$ K (dashed lines). The measured and calculated data confirm that the c/a -ratios of wurtzite InGaN, AlGaN and AlInN crystals are always below the value of an ideal hexagonal crystal with $c/a = 1.633$ [31, 33–35]. (b) The cell internal parameter, u , of random AlGaN, InGaN and AlInN alloys predicted by the theory described in section 2 and approximated by a quadratic equation (11). The nonlinearity of the cell internal parameter in dependence on alloy composition can be described by a negative bowing parameter b , given in the figure. The u parameter of the alloys is always above the value for an ideal hexagonal crystal ($u_{\text{ideal}} = 0.375$).

Table 2. Predicted average (virtual crystal limit) cell internal parameters, lattice constants and cation–anion distances between nearest and second-nearest neighbours (given in Å) as well as bond angles (given in degrees) of ternary random alloys with $x = 0.5$.

	Al _{0.5} Ga _{0.5} N	Al _{0.5} In _{0.5} N	In _{0.5} Ga _{0.5} N
u	0.379	0.378	0.377
a	3.154	3.347	3.392
c/a	1.620	1.612	1.625
M–N _{c1}	1.935	2.042	2.078
M–N _{b1}	1.924	2.041	2.073
M–N _{c2}	3.175	3.354	3.436
M–N _{b2}	3.701	3.921	3.977
M–N _{b'2}	3.694	3.920	3.975
α	108.80	108.76	109.13
β	110.14	110.18	109.81

4. Polarity

An additional important structural property of group III nitrides with wurtzite structure, which strongly affects the orientation of the spontaneous and piezoelectric polarization, is the polarity of the crystals.

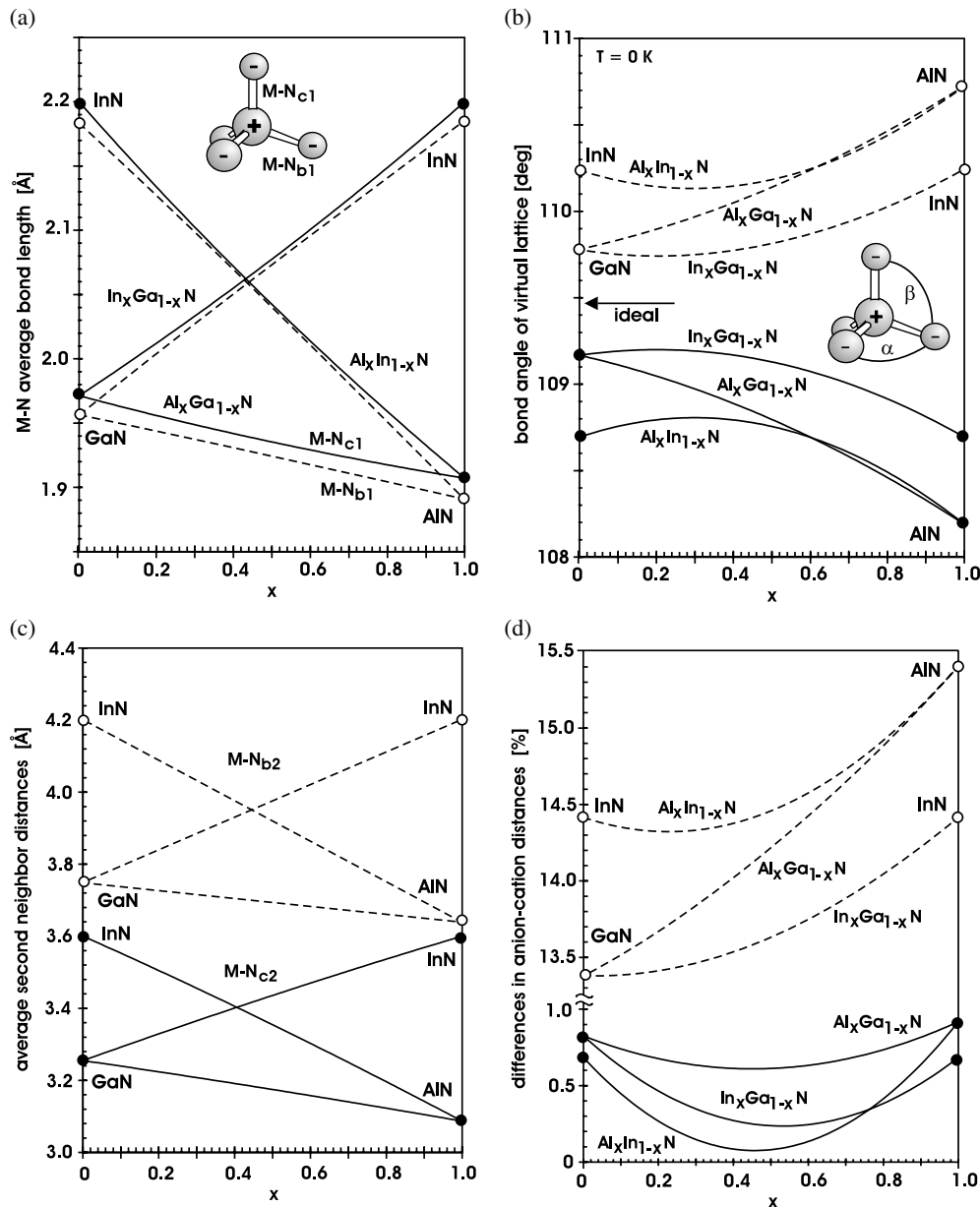


Figure 5. (a) The average bond length (virtual crystal limit) of the metal–nitrogen bond along the c -axis (solid line) and in the direction of the basal plane (dashed line) in dependence on alloy composition. (b) The average bond angles α and β of random AlGaN , InGaN and AlInN alloys versus x . The average bond angles deviate significantly from the bond angle of an ideal hexagonal crystal, where $\alpha = \beta = 109.47^\circ$. The deviation is increasing from GaN to InN and AlN in a nonlinear way. (c) The average second-nearest-neighbour distances of metal and nitrogen atoms in alloys with wurtzite crystal structure versus alloy composition. The second-nearest-neighbour distance along the c -axis is 13–15% shorter than the M-N_{b2} distances along the basal planes (see also tables 1 and 2). (d) The ratios $r = \{1 - (\text{M-N}_{c2}/\text{M-N}_{b2})\}$ between the nearest- and second-nearest-neighbour distances along the c -axis and in the direction of the basal plane are shown in dependence on alloy composition.

Noncentrosymmetric compound crystals exhibit two different sequences of atomic layering in the two opposing directions parallel to certain crystallographic axes. As a consequence, crystallographic polarity along these axes can be observed. For binary A–B compounds with wurtzite structure, the sequence of the atomic layers of the constituents A and B is reversed along the [0001] and [000 $\bar{1}$] directions. The corresponding (0001) and (000 $\bar{1}$) faces are the A-face and B-face, respectively. In the case of heteroepitaxial growth of thin films of a noncentrosymmetric compound, the polarity of the material cannot be predicted in a straightforward way, and must be determined by experiment. This is the case for group III nitrides with wurtzite structure and GaN-based heterostructures with the most common growth direction normal to the {0001} basal plane, where the atoms are arranged in bilayers. These bilayers consist of two closely spaced hexagonal layers, one formed by cations and the other formed by anions, leading to polar faces. Thus, in the case of GaN, a basal surface should be either Ga- or N-face. Ga-face means Ga atoms are placed on the top position of the {0001} bilayer, corresponding to the [0001] polarity (figure 3) (by convention, the [0001] direction is given by a vector pointing from a Ga atom to a nearest-neighbour N atom). It is important to notice that the (0001) and (000 $\bar{1}$) surfaces of GaN are not equivalent and differ in their chemical and physical properties [39].

Both types of polarity were observed by ion channelling and convergent beam electron diffraction in GaN(0001) layers grown by metal–organic chemical vapour deposition (MOCVD) on *c*-plane sapphire if the layers exhibited a rough surface morphology, while for smooth films exclusively Ga-face polarity was shown by the experimental results [40]. This result was supported by a photoelectron diffraction study of MOCVD-grown films [41]. Smith *et al* [42, 43] reported on investigations of surface reconstructions of GaN grown by plasma-induced molecular beam epitaxy (PIMBE) on *c*-plane sapphire and by PIMBE homoepitaxy on a MOCVD-grown GaN/sapphire substrate. They observed two structurally nonequivalent faces with completely different surface reconstructions attributed to the N-face for MBE growth on sapphire and to the Ga-face for MBE deposition on an MOCVD template.

As reported earlier, the polarity of the investigated samples (see section 5) was determined by the x-ray standing wave (XSW) method [44]. The advantage of this technique is the combination of the structural sensitivity of x-ray diffraction with the chemical sensitivity inherent to x-ray spectroscopy. The method is based on generating an XSW field by x-ray Bragg diffraction and monitoring the x-ray fluorescence yield excited by this field as a function of glancing angle as the GaN layer is turned through the narrow region of Bragg reflection. In the case of AlGaN/GaN, InGaN/GaN and AlInN/GaN hetero- and nanostructures grown on *c*-Al₂O₃ substrates covered with a thin AlN nucleation layer the XSW technique was applied successfully. The standing wave was generated by x-ray diffraction inside the GaN buffer and the Ga K α fluorescence yield was recorded as a function of the incident angle within the width of the (0002) reflection peak [45]. In these studies the samples grown by MOCVD as well as by PIMBE on an AlN nucleation layer were determined to exclusively have Ga-face polarity.

5. Growth of undoped AlGaN/GaN, InGaN/GaN and AlInN/GaN hetero- and nanostructures

The investigated pseudomorphic Ga-face AlGaN/GaN, InGaN/GaN and AlInN/GaN heterostructures were grown by low-pressure MOCVD or PIMBE.

(i) *AlGaN/GaN heterostructures.* The MOCVD-grown undoped AlGaN/GaN heterostructures were deposited at a pressure of 100 mbar, using triethylgallium (TEG), trimethylalu-

minium (TMA) and ammonia as precursors. A growth rate of about $0.5 \mu\text{m h}^{-1}$ was achieved for a substrate temperature of 1040°C and V/III gas phase ratios of 1800 and about 900 for GaN and AlGaN, respectively [46]. The AlGaN/GaN heterostructures as well as the $\text{Al}_{0.1}\text{Ga}_{0.9}\text{N}$ nucleation layers were grown at a constant substrate temperature and without any growth interruptions to avoid the presence of excessively high free-carrier background concentrations. $\text{Al}_x\text{Ga}_{1-x}\text{N}$ barriers with thicknesses between 100 and 450 Å and alloy compositions of up to $x = 0.45$ were deposited on GaN buffer layers with thicknesses between 1 and $2.5 \mu\text{m}$.

AlGaN/GaN heterostructures were also deposited by PIMBE using conventional effusion cells and a radio-frequency plasma source for the generation of nitrogen radicals. The nitrogen flux through the plasma source was fixed at about 1 sccm, giving a nitrogen partial pressure in the MBE chamber of 4×10^{-5} mbar during growth. The optimized growth temperature for GaN was determined to be between 780 and 800°C for a Ga flux of $1.5 \times 10^{15} \text{ cm}^{-2} \text{ s}^{-1}$, resulting in a growth rate of $0.5 \mu\text{m h}^{-1}$ as discussed in more detail in [23,47]. AlGaN barriers with thicknesses between 2 and 50 nm were grown on GaN buffer layers using a total flux of Al and Ga atoms equal to the Ga flux optimized for the deposition of high-quality GaN.

(ii) *InGaN/GaN heterostructures.* MOCVD-grown $\text{In}_{0.13}\text{Ga}_{0.87}\text{N}/\text{GaN}$ single-QW structures with well widths from 0.9 to 54 nm were embedded between a $2.7 \mu\text{m}$ thick GaN buffer layer, deposited on top of a low-temperature nucleation layer, and a 130 nm thick GaN cap layer [48,49]. The InGaN layers were grown at a substrate temperature of 770°C , which is 360°C lower than for the growth of GaN. The InGaN composition and layer thickness were determined by a combination of secondary-ion mass spectroscopy (SIMS), HRXRD and Raman spectroscopy.

(iii) *AlInN/GaN heterostructures.* $\text{Al}_{1-x}\text{In}_x\text{N}/\text{GaN}/\text{AlN}$ (50/540/80 nm) heterostructures with In concentrations between $x = 0.12$ and 0.21 in the barrier were also grown by MOCVD [50]. The AlN nucleation layer, GaN buffer layer and AlInN barrier were deposited at substrate temperatures of 900, 1000 and 750°C , respectively. The In concentration of the barrier was increased by increasing the flux of the indium precursor (trimethylindium, TMIIn) from 7.5 to $42 \mu\text{mol min}^{-1}$, keeping the flux of the aluminium precursor (TMAI), the transport gas N_2 and the ammonia constant at $3.4 \mu\text{mol min}^{-1}$, 2000 and 4250 sccm, respectively.

Before we discuss the experimentally observed polarization-induced effects in these hetero- and nanostructures we shall provide the theoretical background for a detailed understanding of nonlinear spontaneous and piezoelectric polarization in binary and ternary group III nitrides.

6. Nonlinear spontaneous and piezoelectric polarization in group III nitrides

Models of polarization-induced effects in GaN-based electronic and optoelectronic devices so far have assumed that polarization in ternary nitride alloys interpolates linearly between the limiting values determined by the binary compounds. It is known from earlier work on III-V alloys with zincblende structure that, although Vegard's law is found to be valid in predicting the macroscopic structural properties of alloys (a and c lattice constants in this context), the electronic properties such as the bandgap are nonlinear functions of the alloy composition. These nonlinearities can be caused by different response to the hydrostatic compression of the binary constituents, charge transfer between cations due to different electronegativity, internal strain effects due to varying cation-anion bond length (bond alternation) and disorder effects due to random distribution of the chemical elements on the cation side.

6.1. Spontaneous polarization

Motivated by the observed nonlinearities in the internal structural parameters (u parameter in this context), we have recently investigated the pyroelectric properties of alloys looking for possible nonlinearities [38]. The results show that the spontaneous polarization of relaxed alloys for a given composition depends linearly on the average u parameter, which indicates that spontaneous polarization differences between alloys of the same composition are mainly due to varying cation–anion bond length, whereas disorder has a negligible influence. This idea is supported by the fact that in binaries the polarization depends linearly on the relative displacement of the cation and anion sub-lattices in the [0001] direction [1]. Because of the nonlinear dependence of the cell internal parameter on alloy composition a nonlinear behaviour of the spontaneous polarization versus x has to be expected.

Superimposed on the nonlinearities which are caused by the structural properties, Bernardini *et al* pointed out that the different response to the hydrostatic pressure of the binary constituents of the alloy should contribute significantly to the nonlinear behaviour of spontaneous polarization in ternary random alloys [1, 2, 35].

Using the theoretical approach described in section 2 we have calculated the spontaneous polarization of relaxed $A_{0.5}B_{0.5}N$ alloys (listed in table 2) in order to determine the bowing parameter of P_{ABN}^{SP} as a function of x . The spontaneous polarization of the random ternary nitride alloys is given to second order in x by (in $C\ m^{-2}$)

$$\begin{aligned} P_{ABN}^{SP}(x) &= P_{AN}^{SP}x + P_{BN}^{SP}(1-x) + bx(1-x) \\ P_{AlGaN}^{SP}(x) &= -0.090x - 0.034(1-x) + 0.021x(1-x) \\ P_{InGaN}^{SP}(x) &= -0.042x - 0.034(1-x) + 0.037x(1-x) \\ P_{AlInN}^{SP}(x) &= -0.090x - 0.042(1-x) + 0.070x(1-x). \end{aligned} \quad (13)$$

The first two terms in the equations are the usual linear interpolation between the binary compounds. The third term embodies nonlinearity to quadratic order (see also figure 6). Higher-order terms are neglected as their effect was estimated to be less than 10%.

Knowledge of the spontaneous polarization in alloys is not sufficient to describe the pyroelectric properties of alloys and GaN-based nanostructures or to predict the values of polarization-induced interface charges and electrostatic fields. GaN-based hetero- and nanostructures are usually grown pseudomorphically and strained on substrates and buffer layers with significant mismatch in lattice constants and thermal expansion coefficients. The ensuing symmetry conserving strain causes a change in the crystal structure and in polarization that amounts to a piezoelectric polarization. Therefore the polarization of every layer is a combination of spontaneous and piezoelectric components.

6.2. Piezoelectric polarization

By Hooke's law the deformation of a crystal ε_{kl} , due to external or internal forces or stresses σ_{ij} , can be described by

$$\sigma_{ij} = \sum_{k,l} C_{ijkl} \varepsilon_{kl} \quad (14)$$

where C_{ijkl} is the elastic tensor. Due to spatial symmetry this fourth-rank tensor can be reduced to a 6×6 matrix using the Voigt notation: $xx \rightarrow 1$, $yy \rightarrow 2$, $zz \rightarrow 3$, $yz, zy \rightarrow 4$, $zx, xz \rightarrow 5$, $xy, yx \rightarrow 6$. The elements of the elastic tensor can be rewritten as $C_{ijkl} = C_{mn}$, where $i, j, k, l = x, y, z$ and $m, n = 1, \dots, 6$. Using this notation, Hooke's law can be

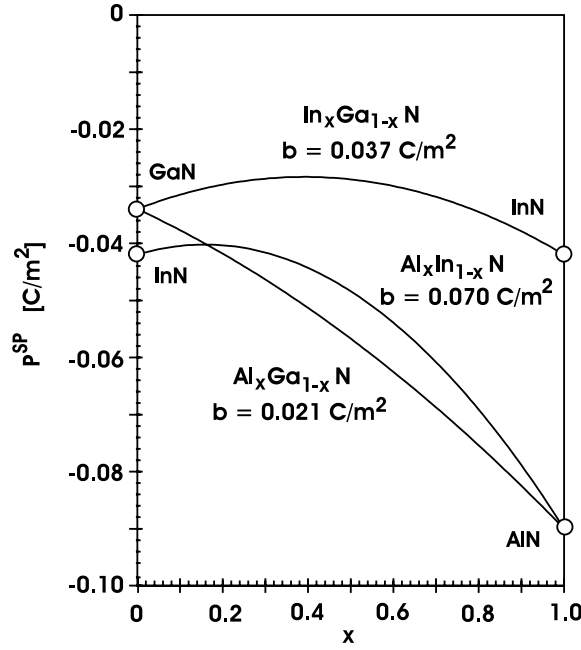


Figure 6. Predicted spontaneous polarization for random, ternary alloys with wurtzite crystal structure. The dependence of P^{SP} on x can be approximated with high accuracy by quadratic equations (13). The nonlinearity can be described by positive bowing parameters increasing from AlGaIn to InGaIn and AlInN.

simplified to

$$\sigma_i = \sum_j C_{ij} \varepsilon_j. \quad (15)$$

The 6×6 matrix of the elastic constants C_{ij} (see table 3 [51, 52]) for crystals with wurtzite structure is given by

$$C_{ij} = \begin{pmatrix} C_{11} & C_{12} & C_{13} & 0 & 0 & 0 \\ C_{12} & C_{11} & C_{13} & 0 & 0 & 0 \\ C_{13} & C_{13} & C_{33} & 0 & 0 & 0 \\ 0 & 0 & 0 & C_{44} & 0 & 0 \\ 0 & 0 & 0 & 0 & C_{44} & 0 \\ 0 & 0 & 0 & 0 & 0 & \frac{1}{2}(C_{11} - C_{12}) \end{pmatrix}. \quad (16)$$

Another useful way to describe the mechanical properties of the crystals is the elastic compliance constants. These parameters are calculated by inversion of the C_{ij} matrix to

$$S_{11} = \frac{C_{11}C_{33} - C_{13}^2}{(C_{11} - C_{12})[C_{33}(C_{11} + C_{12}) - 2C_{13}^2]} \quad (17)$$

$$S_{12} = -\frac{C_{12}C_{33} - C_{13}^2}{(C_{11} - C_{12})[C_{33}(C_{11} + C_{12}) - 2C_{13}^2]} \quad (18)$$

$$S_{13} = -\frac{C_{13}}{C_{33}(C_{11} + C_{12}) - 2C_{13}^2} \quad (19)$$

$$S_{33} = \frac{C_{11} + C_{12}}{C_{33}(C_{11} + C_{12}) - 2C_{13}^2} \quad (20)$$

Table 3. Experimental and predicted elastic compliance, elastic constants and piezoelectric constants as well as the Poisson number of wurtzite binary group III nitrides at room temperature (theory 1 [51], theory 2 [1,2]).

Hexagonal crystal property	InN		GaN			AlN		
	Theory 1	Theory 2	Theory 1	Theory 2	Exp.	Theory 1	Theory 2	Exp.
C_{11} (GPa)	223		367		370 ^a	396		410 ^a
C_{12} (GPa)	115		135		145 ^a	137		140 ^a
C_{13} (GPa)	92	70	103	68	110 ^a	108	94	100 ^a
C_{33} (GPa)	224	205	405	354	390 ^a	373	377	390 ^a
C_{44} (GPa)	48		95		90 ^a	116		120 ^a
$\nu(0001)$	0.82	0.68	0.52	0.38	0.56	0.58	0.50	0.51
S_{11} (10^{-12} N m ⁻²)	6.535		3.267		3.326	2.993		2.854
S_{12} (10^{-12} N m ⁻²)	-2.724		-1.043		-1.118	-0.868		-0.849
S_{13} (10^{-12} N m ⁻²)	-1.565		-0.566		-0.623	-0.615		-0.514
S_{33} (10^{-12} N m ⁻²)	5.750		2.757		2.915	3.037		2.828
S_{44} (10^{-12} N m ⁻²)	20.83		10.53		11.11	8.621		8.333
e_{31} (C m ⁻²)		-0.41		-0.34			-0.53	-0.58 ^d
e_{33} (C m ⁻²)		0.81		0.67			1.50	1.55 ^d
e_{15} (C m ⁻²)			-0.22 ^b		-0.30 ^c			-0.48 ^d
d_{31} (10^{-12} C m ⁻² Pa)		-3.147		-1.253			-2.298	-2.65
d_{33} (10^{-12} C m ⁻² Pa)		6.201		2.291			5.352	5.53
d_{15} (10^{-12} C m ⁻² Pa)		-2.292		-1.579			-2.069	-4.08

^a Experimental results from [10].

^b Experimental results from [7].

^c Experimental results from [52].

^d Experimental results from [11].

and

$$S_{44} = \frac{1}{C_{44}}. \quad (21)$$

Using the compliance constants, a helpful figure of merit to determine the directional hardness and the reciprocal Young's modulus as a function of orientation to the crystal axis can be provided. For hexagonal materials the reciprocal Young's modulus S_{11}^* along an arbitrary direction at an angle θ with respect to the [0001]-axis is given by [53,54]

$$S_{11}^* = S_{11} \sin^4(\theta) + S_{33} \cos^4(\theta) + (S_{44} + 2S_{13}) \sin^2(\theta) \cos^2(\theta). \quad (22)$$

In figures 7(a) and (b) polar plots of S_{11}^* for InN, GaN and AlN as a function of the direction with respect to the [0001]-axis and for directions along the basal plane are shown. It is seen that AlN and GaN are more than twice as hard as InN. The hardness of AlN is almost isotropic whereas GaN and InN show preferential 'softness' along the [0001]- and $[2\bar{1}10]$ -axes. Of main interest here is the fact that the hardness of all binary compounds with wurtzite structure is isotropic in the basal plane. This is important because the strain in epitaxial layers of group III nitride heterostructures grown along the c -axis ([0001]-axis) caused by mismatch of the lattice constants a and/or a mismatch of the thermal expansion coefficients of layer and substrate is directed along the basal plane (parallel to the substrate). No force is applied in the growth direction and the crystal can relax freely in this direction. The resulting biaxial strain ($\varepsilon_1 = \varepsilon_2$) causes stresses $\sigma_1 = \sigma_2$, whereas σ_3 has to be zero. Using equations (15) and (16), a relation between the strain along the c -axis and along the basal plane can be derived:

$$\varepsilon_3 = -2 \frac{C_{13}}{C_{33}} \varepsilon_1 \quad (23)$$

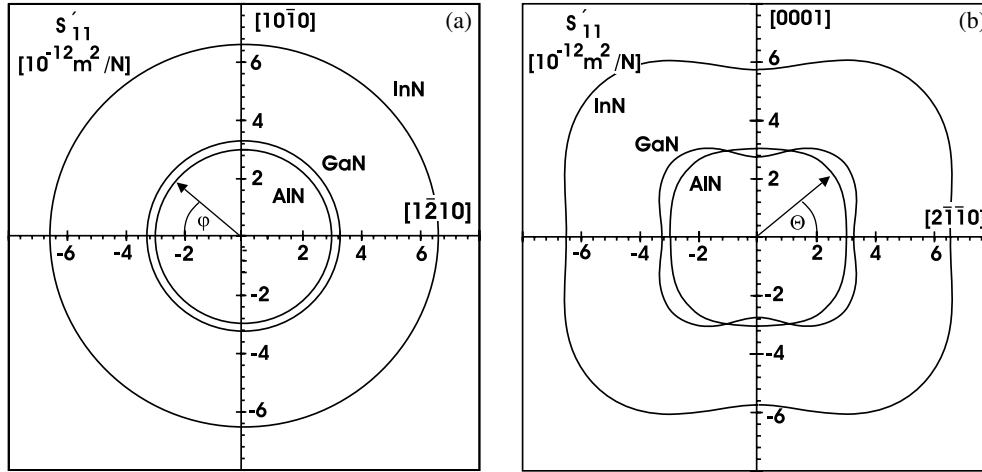


Figure 7. (a) The reciprocal Young's moduli in the basal plane of InN, GaN and AlN. The stiffness of AlN and GaN is more than twice that for InN. More important, the hardness of the wurtzite crystals is isotropic in the basal plane. (b) The reciprocal Young's modulus along an arbitrary direction at an angle θ with respect to the c -axis. In this plane the stiffness of AlN is isotropic whereas GaN and InN show preferential 'softness' along the $[0001]$ - and $[2\bar{1}\bar{1}0]$ -directions.

where

$$\nu(0001) = 2 \frac{C_{13}}{C_{33}} \quad (24)$$

is the Poisson ratio and

$$\varepsilon_1 = \frac{a - a_0}{a_0} \quad \varepsilon_3 = \frac{c - c_0}{c_0} \quad (25)$$

are the relative changes of the lattice constants a and c with respect to the constants of the relaxed crystals a_0 and c_0 . The stresses in the basal plane caused by the mismatch in the lattice constants can be calculated by

$$\sigma_1 = \varepsilon_1 \left(C_{11} + C_{12} - 2 \frac{C_{13}^2}{C_{33}} \right) \quad (26)$$

where

$$C_{11} + C_{12} - 2 \frac{C_{13}^2}{C_{33}} > 0. \quad (27)$$

The piezoelectric polarization for hexagonal materials belonging to the C_{6v} crystallographic point group [53] is given by

$$P_i^{\text{pz}} = \sum_l d_{il} \sigma_l \quad i = 1, 2, 3 \quad l = 1, \dots, 6 \quad (28)$$

where P_i^{pz} are the components of the piezoelectric polarization and d_{il} are the piezoelectric moduli (table 3). Using the symmetry relations between the piezoelectric moduli, $d_{31} = d_{32}$, $d_{33} \neq 0$ and $d_{15} = d_{24}$ (all other components $d_{il} = 0$), equation (28) can be reduced to a set of three equations:

$$P_1^{\text{pz}} = \frac{1}{2} d_{15} \sigma_5 \quad (29)$$

$$P_2^{\text{pz}} = \frac{1}{2} d_{15} \sigma_4 \quad (30)$$

$$P_3^{\text{pz}} = d_{31} (\sigma_1 + \sigma_2) + d_{33} \sigma_3. \quad (31)$$

Keeping in mind that for biaxial stress, as is of interest here, $\sigma_1 = \sigma_2$, $\sigma_3 = 0$ and shear stresses are assumed to be negligible ($\sigma_4 = \sigma_5 = 0$), the piezoelectric polarization has only one non-vanishing component, which is directed along the growth direction and is given by

$$P_3^{\text{PZ}} = 2d_{31}\sigma_1 = 2d_{31}\varepsilon_1 \left(C_{11} + C_{12} - 2\frac{C_{13}^2}{C_{33}} \right). \quad (32)$$

More often than the piezoelectric moduli, the piezoelectric constants e_{kl} are used to describe the piezoelectric properties of group III nitrides. They can be calculated by

$$e_{kl} = \sum_j d_{kj}C_{jl} \quad \text{where } k = 1, 2, 3 \quad l = 1, \dots, 6 \quad j = 1, \dots, 6. \quad (33)$$

For hexagonal crystals the relations between piezoelectric constants and moduli can be reduced to

$$e_{31} = e_{32} = C_{11}d_{31} + C_{12}d_{32} + C_{13}d_{33} = (C_{11} + C_{12})d_{31} + C_{13}d_{33} \quad (34)$$

$$e_{33} = 2C_{13}d_{31} + C_{33}d_{33} \quad (35)$$

$$e_{15} = e_{24} = C_{44}d_{15} \quad (36)$$

and

$$e_{kl} = 0 \quad \text{for all other components.} \quad (37)$$

The piezoelectric polarization as a function of strain can be written as

$$P_k^{\text{PZ}} = \sum_l e_{kl}\varepsilon_l \quad \text{where } k = 1, 2, 3 \quad l = 1, \dots, 6. \quad (38)$$

The nonvanishing component of the piezoelectric polarization caused by biaxial strain is

$$P_3^{\text{PZ}} = \varepsilon_1 e_{31} + \varepsilon_2 e_{32} + \varepsilon_3 e_{33} \quad (39)$$

$$= 2\varepsilon_1 e_{31} + \varepsilon_3 e_{33} \quad \text{where } \varepsilon_3 = -2\frac{C_{13}}{C_{33}}\varepsilon_1 \quad (40)$$

$$= 2\varepsilon_1 \left(e_{31} - e_{33} \frac{C_{13}}{C_{33}} \right). \quad (41)$$

It is interesting to note that, besides the fact that the piezoelectric polarization along the c -axis is linearly dependent on the relative change of the lattice constant a , P_3^{PZ} is always negative for layers under biaxial tensile strain and positive for crystals under compressive strain. As a consequence, the spontaneous and the piezoelectric polarization are pointing along the $[000\bar{1}]$ -direction for biaxial tensile strained layers, whereas in crystals under biaxial compressive strain the piezoelectric polarization is oriented along the $[0001]$ -axis (anti-parallel to the spontaneous polarization).

Because of its relevance for nitride-based devices we have determined P_3^{PZ} (we shall omit the index 3 in the following discussion) for alloys pseudomorphically grown on relaxed InN, GaN and AlN buffer layers. Under these assumptions, the strain can be calculated by

$$\varepsilon_1 = \frac{a_{\text{buffer}} - a(x)}{a(x)}. \quad (42)$$

As a first approach, the lattice (see equations (4)), piezoelectric and elastic constants of the alloys are approximated by a linear interpolation between the constants of the relevant binary compounds and implemented in equation (41). For the following calculations we have used the physical properties of the binary compounds predicted by Zoroddu *et al* (table 3, theory 2) [2]. Figures 8(a)–(c) show the piezoelectric polarization of the alloys pseudomorphically grown on binary buffer layers for different values of x . Very high values of piezoelectric polarization

covering the range from -0.28 (AlN/InN) to 0.182 C m^{-2} (InN/AlN) are observed. In addition, it should be pointed out that the piezoelectric polarization P^{pz} , calculated with the same piezoelectric constants as before but using the elastic constants predicted by Wright (table 3, theory 1) or measured by Deger *et al* [10], deviates from the values shown in figures 8(a)–(c) by only 10% in the worst case (AlN/InN heterostructure).

As a consequence of equation (41) and the linear interpolation of the elastic and piezoelectric constants, the piezoelectric polarization is nonlinear in terms of the alloy composition. The nonlinear dependence of the piezoelectric polarization on the alloy composition can be approximated with an accuracy of better than 1% by the following quadratic equations:

$$\begin{aligned} P_{\text{AlGaIn}/\text{InN}}^{\text{pz}}(x) &= [-0.28x - 0.113(1-x) + 0.042x(1-x)] \text{C m}^{-2} \\ P_{\text{AlGaIn}/\text{GaN}}^{\text{pz}}(x) &= [-0.0525x + 0.0282x(1-x)] \text{C m}^{-2} \\ P_{\text{AlGaIn}/\text{AlN}}^{\text{pz}}(x) &= [0.026(1-x) + 0.0248x(1-x)] \text{C m}^{-2} \end{aligned} \quad (43)$$

$$\begin{aligned} P_{\text{InGaIn}/\text{InN}}^{\text{pz}}(x) &= [-0.113(1-x) - 0.0276x(1-x)] \text{C m}^{-2} \\ P_{\text{InGaIn}/\text{GaN}}^{\text{pz}}(x) &= [0.148x - 0.0424x(1-x)] \text{C m}^{-2} \\ P_{\text{InGaIn}/\text{AlN}}^{\text{pz}}(x) &= [0.182x + 0.026(1-x) - 0.0456x(1-x)] \text{C m}^{-2} \end{aligned} \quad (44)$$

$$\begin{aligned} P_{\text{AlInN}/\text{InN}}^{\text{pz}}(x) &= [-0.28x + 0.104x(1-x)] \text{C m}^{-2} \\ P_{\text{AlInN}/\text{GaN}}^{\text{pz}}(x) &= [-0.0525x + 0.148(1-x) + 0.0938x(1-x)] \text{C m}^{-2} \\ P_{\text{AlInN}/\text{AlN}}^{\text{pz}}(x) &= [0.182(1-x) + 0.092x(1-x)] \text{C m}^{-2}. \end{aligned} \quad (45)$$

For heterostructures with barriers under moderate strain, these equations can be used as an input, either directly as polarization or, as discussed in more detail later, as interface-bound sheet charge, depending on the implementation, in a self-consistent Schrödinger–Poisson solver based for example on effective-mass or tight-binding theory.

Up to now, we have relied on Hooke's law assuming that C_{ij} and e_{ij} are constant for a given binary or ternary crystal and that the piezoelectric polarization depends linearly on the strain, but it is known from other piezoelectric semiconductors that, if high forces or pressures are applied to the crystals, this relation can become nonlinear [55]. In the following, we first demonstrate that the piezoelectricity of GaN, InN and AlN as well as nitride alloys is nonlinear in terms of strain, then we suggest how to use this understanding in practice for an improved prediction of the piezoelectric polarization of random alloys caused by high biaxial strain. We consider the technologically most relevant case of an alloy pseudomorphically grown on an unstrained GaN buffer layer. Using the same theoretical approach as described in section 2, we calculate the polarization with the constraint $a_{\text{buffer}} = a_{\text{GaN}}$, reoptimizing all structures. The piezoelectric polarization is then computed as the difference of the total polarization obtained from this calculation and the spontaneous polarization.

Figures 9(a) and (b) show the piezoelectric polarization versus strain calculated by equation (41) (linear in strain) and our improved theoretical approach for binary compounds. In both cases the piezoelectric polarization for a given strain increases from GaN to InN and AlN. It is important that calculations by our improved method lead to significantly higher piezoelectric polarizations, especially in cases of high strains (high In concentrations). The calculated nonlinear piezoelectricity of the binary compounds can be described by the relations (in C m^{-2}):

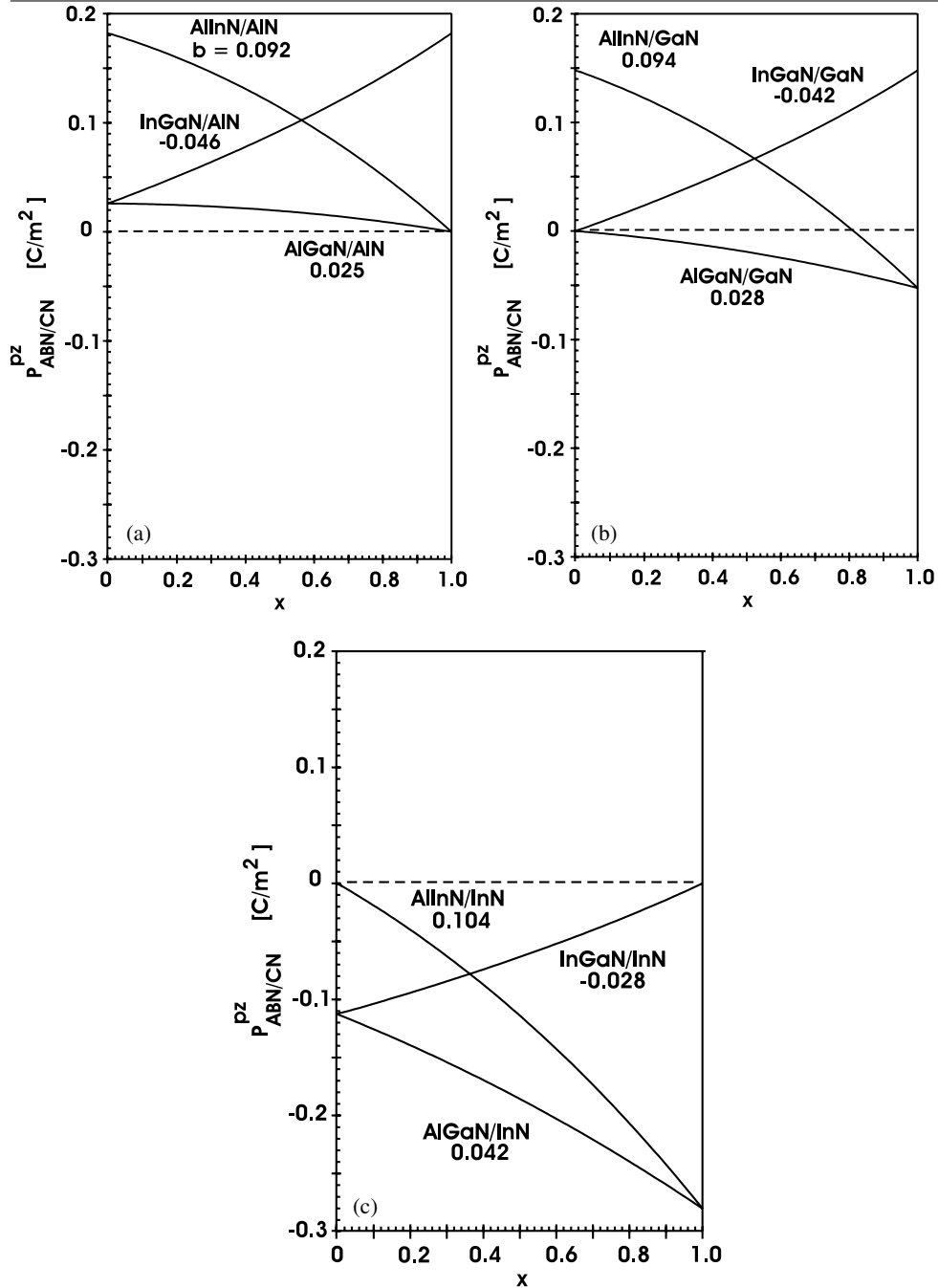


Figure 8. (a) The piezoelectric polarization of ternary alloys pseudomorphically grown on relaxed AlN buffer layers. For ternary alloys grown on AlN the positive piezoelectric polarization is oriented anti-parallel to the negative spontaneous polarization. The bowing parameters describing the nonlinearity of P^{pz} in dependence on x are given in addition. (b) The piezoelectric polarization of ternary alloys pseudomorphically grown on relaxed GaN buffer layers. For lattice-matched $Al_{0.82}In_{0.18}N/GaN$ heterostructures the piezoelectric polarization is equal to zero. (c) The piezoelectric polarization of ternary alloys pseudomorphically grown on relaxed InN buffer layers. For ternary alloys grown on InN the negative piezoelectric polarization is oriented parallel to the spontaneous polarization along the c -axis.

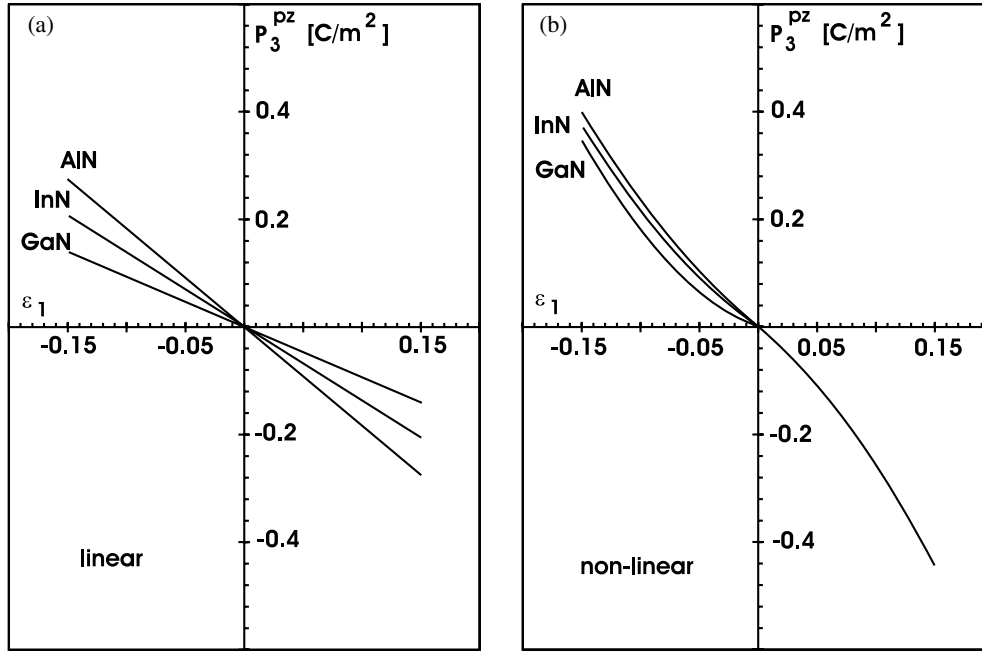


Figure 9. (a) The piezoelectric polarization of binary group III nitrides with wurtzite structure under biaxial tensile or compressive strain calculated by equation (41). The value of the piezoelectric polarization is increasing linearly with increasing strain and for a given biaxial strain from GaN to InN and AlN. (b) The piezoelectric polarization of binary group III nitrides with wurtzite structure under biaxial tensile or compressive strain calculated by the theory described in section 2. The value of piezoelectric polarization is increasing nonlinearly with increasing strain, exceeding the values calculated by equation (41).

$$P_{\text{AlN}}^{\text{pz}} = -1.808\epsilon + 5.624\epsilon^2 \quad \text{for } \epsilon < 0 \quad (46a)$$

$$P_{\text{AlN}}^{\text{pz}} = -1.808\epsilon - 7.888\epsilon^2 \quad \text{for } \epsilon > 0 \quad (46b)$$

$$P_{\text{GaN}}^{\text{pz}} = -0.918\epsilon + 9.541\epsilon^2 \quad (46c)$$

$$P_{\text{InN}}^{\text{pz}} = -1.373\epsilon + 7.559\epsilon^2. \quad (46d)$$

The observed nonlinearity in the bulk piezoelectricity exceeds any effects related to disorder or bond alternation which were taken into account [38]. Therefore, the calculation of the piezoelectric polarization of an $A_xB_{1-x}N$ alloy at any strain becomes straightforward. One can choose a value for x , calculate the strain $\epsilon_1 = \epsilon(x)$ from Vegard's law, and the piezoelectric polarization by

$$P_{\text{ABN}}^{\text{pz}}(x) = xP_{\text{AN}}^{\text{pz}}(\epsilon(x)) + (1-x)P_{\text{BN}}^{\text{pz}}(\epsilon(x)) \quad (47)$$

where $P_{\text{AN}}^{\text{pz}}(\epsilon(x))$, $P_{\text{BN}}^{\text{pz}}(\epsilon(x))$ are the strain-dependent bulk piezoelectric polarizations of the relevant binary compounds given above. The piezoelectric and spontaneous polarizations of random ternary AlGaIn, InGaIn and AlInIn alloys pseudomorphically grown on relaxed GaN buffer layers are shown in figures 10 and 6, respectively. The piezoelectric polarization changes nonlinearly with alloy composition, reaching the lowest and highest value of -0.461 and 0.315 C m^{-2} for pseudomorphic AlN/InN and InN/AlN heterostructures, respectively. Especially for alloys with high indium concentration, which are, however, difficult to realize in practice, the value of the piezoelectric polarization exceeds that of the spontaneous polarization. It is interesting to note that $\text{Al}_{0.82}\text{In}_{0.18}\text{N}/\text{GaN}$ heterostructures are predicted to grow lattice

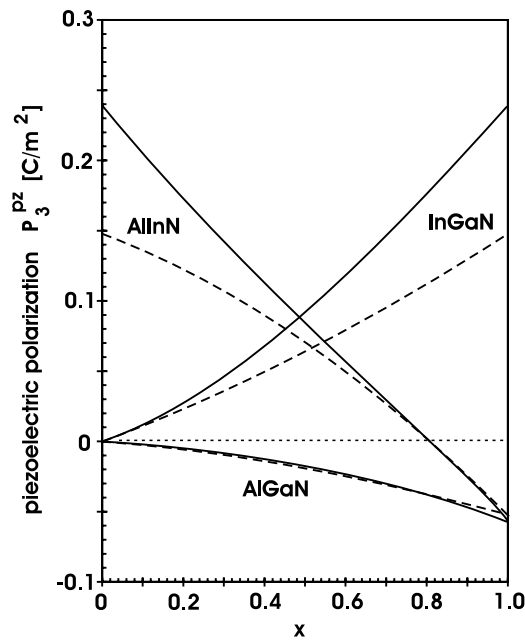


Figure 10. The piezoelectric polarization of random ternary alloys pseudomorphically grown on relaxed GaN buffer layers calculated by (i) equation (41) and using linear interpolations of the physical properties (e_{xy} , C_{xy}) for the relevant binary compounds (dashed curves); (ii) taking into account the nonlinearity in the piezoelectric polarization in terms of strain (equations (46)) (solid curves). For alloys under high biaxial strain (layers with high In concentration) the piezoelectric polarization is underestimated by approach (i).

matched and the piezoelectric polarization in the alloy should vanish in this case. A comparison of the calculated values of P^{Pz} using a linear interpolation of the elastic and piezoelectric constants or taking the nonlinearity of the piezoelectric polarization into account shows that the linear interpolation leads to an underestimation of the piezoelectric polarization. Therefore, the improved scheme represented by equations (46) and (47) is of interest in modelling hetero- and nanostructures with highly strained InGaN and AlInN layers.

7. Polarization-induced surface and interface charges

Based on a theoretical understanding of the nonlinear dependence of spontaneous and piezoelectric polarization on composition and strain we can provide a more accurate prediction of polarization-induced charges bound at surfaces and interfaces of $A_xB_{1-x}N/GaN$ heterostructures.

As mentioned above, the total polarization P is the sum of the piezoelectric and spontaneous polarization,

$$P_{ABN} = P_{ABN}^{Pz} + P_{ABN}^{SP}. \quad (48)$$

Associated with a gradient of polarization in space is a polarization-induced charge density given by

$$\rho_P = -\nabla P. \quad (49)$$

As a special case, at the surface of a relaxed or strained $A_xB_{1-x}N$ layer, as well as at the interfaces of a $A_xB_{1-x}N/GaN$ heterostructure, the total polarization changes abruptly, causing

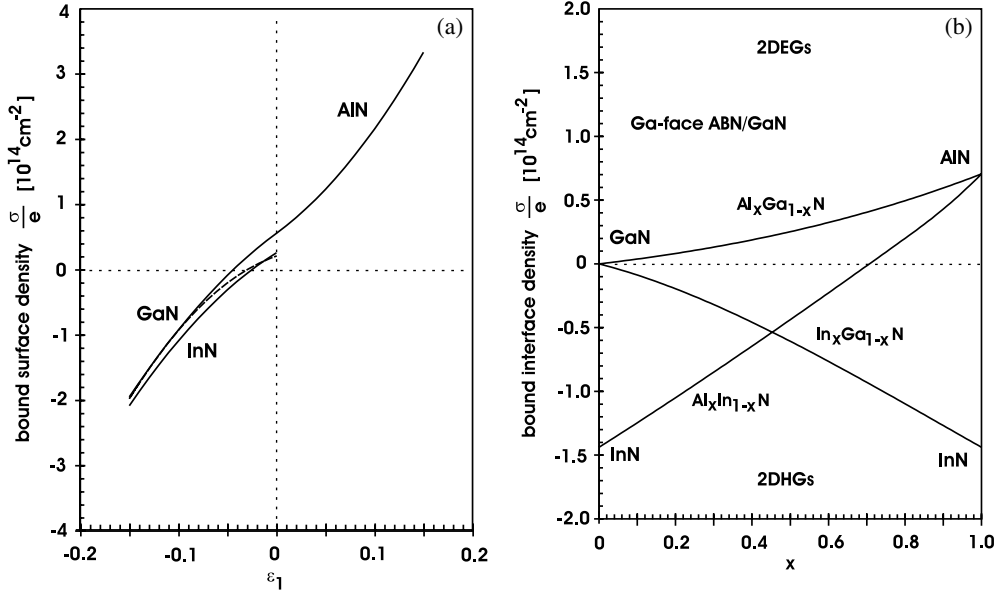


Figure 11. (a) Bound surface density of wurtzite GaN, InN and AlN crystals caused by a gradient in piezoelectric and spontaneous polarization at the surfaces in dependence of biaxial strain applied in the basal plane. (b) Bound interface density of pseudomorphic AlGaN/GaN, InGaN/GaN and AlInN/GaN heterostructures grown on relaxed GaN buffer layers with Ga-face polarity. Positive (negative) polarization-induced interface charges are screened by electrons (holes) in n-type (p-type) samples, causing the formation of two-dimensional carrier gases.

a fixed two-dimensional polarization charge density σ , given by

$$\begin{aligned} \sigma_{\text{ABN}} &= P_{\text{ABN}} = P_{\text{ABN}}^{\text{SP}} + P_{\text{ABN}}^{\text{PZ}} && \text{for surfaces} \\ \sigma_{\text{ABN/GaN}} &= P_{\text{GaN}} - P_{\text{ABN}} && \\ &= (P_{\text{GaN}}^{\text{SP}} + P_{\text{GaN}}^{\text{PZ}}) - (P_{\text{ABN}}^{\text{SP}} + P_{\text{ABN}}^{\text{PZ}}) && \text{for interfaces} \end{aligned} \quad (50)$$

respectively. Figures 11(a) and (b) show the polarization-induced surface and interface sheet density σ/e ($e = -1.602 \times 10^{-19}$ C) for relaxed and strained binary nitrides as well as for pseudomorphic $\text{A}_x\text{B}_{1-x}\text{N}/\text{GaN}$ heterostructures.

The (spontaneous) polarization-induced bound surface density of relaxed InN, GaN and AlN crystals is determined to be 2.62×10^{13} , 2.12×10^{13} and $5.62 \times 10^{13} \text{ cm}^{-2}$, respectively, which is equivalent to approximately two and five electron charges per every 100 surface atoms. If a biaxial compressive strain of e.g. $\varepsilon_1 = -0.02$ is applied to the crystals, the surface charges are reduced to 0.72×10^{13} , 0.74×10^{13} and $3.22 \times 10^{13} \text{ cm}^{-2}$, respectively (figure 11(a)). For compressive strains in InN, GaN and AlN of $\varepsilon_1 = -0.025$, -0.030 and -0.045 the piezoelectric polarization compensates the spontaneous polarization and the strained crystals should be without surface charge and internal electric field. As can be seen from figure 11(a), compressive strain reduces and tensile strain enhances the bound surface charge. It should be mentioned that for relaxed layers grown along the c -axis on a substrate of choice, the surface charge is positive (negative) for material with N-face (Ga-face) polarity.

As in ferroelectrics, the bound surface charge can be screened by oppositely charged surface defects and adsorbed charges from the environment [56]. If the screening of the surface charge by defects or the ambient is not complete, the carrier concentration profiles inside the crystals will be affected [57]. For example in slightly n-type doped Ga-face GaN

grown on *c*-Al₂O₃ substrates free electrons are expected to accumulate at the GaN/Al₂O₃ interface compensating the positive bound (mainly spontaneous) polarization-induced interface charge $+\sigma$, whereas the negative surface charge on top of the GaN layer $-\sigma$ is only partially compensated by the ionized donors. As a consequence a significant band bending at the Ga-face GaN surface is expected.

Since screening by charges from the ambient at A_xB_{1-x}N/GaN interfaces can be excluded, polarization-induced effects are much easier to study in heterostructures in comparison with single epitaxial layers. For pseudomorphic Ga-face Al_xGa_{1-x}N/GaN ($0 < x \leq 1$) and Al_xIn_{1-x}N/GaN ($0.71 < x \leq 1$) heterostructures, the polarization-induced interface charges are predicted to be positive (figure 11(b)). In both cases the bound charge increases nonlinearly with x up to $7.06 \times 10^{13} \text{ cm}^{-2}$, estimated for the AlN/GaN heterostructure. For Ga-face In_xGa_{1-x}N/GaN ($0 < x \leq 1$) and Al_xIn_{1-x}N/GaN ($0 < x \leq 0.71$) heterostructures σ is found to be negative. Again the polarization-induced interface density changes in a nonlinear manner if the alloy composition is varied. For pseudomorphic InN/GaN heterostructures a very high value of the bound sheet density of $14.4 \times 10^{13} \text{ cm}^{-2}$ is calculated.

In n-type heterostructures it has to be taken into account that free electrons will accumulate at interfaces with positive bound sheet charges, compensating $+\sigma$. As a consequence a 2DEG with a sheet carrier concentration close to the concentration of the bound interface density $+\sigma/e$ can be formed. It should be pointed out that these 2DEGs are realized without any need of a modulation-doped barrier. This is of special interest for the fabrication of high-frequency and high power HEMTs, as the growth and processing of these devices is significantly simplified.

8. Sheet carrier concentrations of polarization-induced 2DEGs

With a theoretical understanding of the polarization-induced charge we now can predict the sheet carrier concentration of polarization-induced 2DEGs and their dependence on alloy composition for pseudomorphic Ga-face AlGaN/GaN and AlInN/GaN ($0.71 < x \leq 1$) heterostructures.

For undoped pseudomorphic Ga-face AlGaN/GaN or AlInN/GaN HEMT structures, the sheet electron concentration, $n_s(x)$, can be approximated by taking advantage of the total bound sheet charge $\sigma_{\text{ABN/GaN}}(x)$ calculated above, and the following equation [58]:

$$n_s(x) = \frac{\sigma_{\text{ABN/GaN}}(x)}{e} - \frac{\varepsilon_0 E_F}{e^2} \left(\frac{\varepsilon_{\text{ABN}}(x)}{d_{\text{ABN}}} + \frac{\varepsilon_{\text{GaN}}}{d_{\text{GaN}}} \right) - \frac{\varepsilon_0 \varepsilon_{\text{ABN}}(x)}{e^2 d_{\text{ABN}}} (e\phi_{\text{ABN}}(x) + \Delta(x) - \Delta E_{\text{ABN}}^C(x)) \quad (51)$$

where ε_0 is the dielectric constant of the vacuum, ε_{GaN} and $\varepsilon_{\text{ABN}}(x)$ are the relative dielectric constants of the constituent layers and d_{ABN} and d_{GaN} are the thicknesses of the barrier and the buffer layer, respectively. E_F is the position of the Fermi level with respect to the GaN conduction-band edge close to the GaN/substrate interface, $e\phi_{\text{ABN}}(x)$ is the Schottky barrier height of the gate contact on top of the barrier (used for *C-V*-profiling measurements), $\Delta E_{\text{ABN}}^C(x)$ is the conduction band offset and $\Delta(x)$ is the penetration of the conduction band edge below the Fermi level at the ABN/GaN interface (see figure 12(a)). This latter quantity is calculated by

$$\Delta(x) = E_0(x) + \frac{\pi \eta^2}{m_{\text{GaN}}^*} n_s(x) \quad (52)$$

where the lowest subband level of the 2DEG is given by

$$E_0(x) = \left\{ \frac{9\pi \eta e^2}{8\varepsilon_0 \sqrt{8m_{\text{GaN}}^*}} \frac{n_s(x)}{\varepsilon_{\text{GaN}}} \right\}^{2/3}. \quad (53)$$

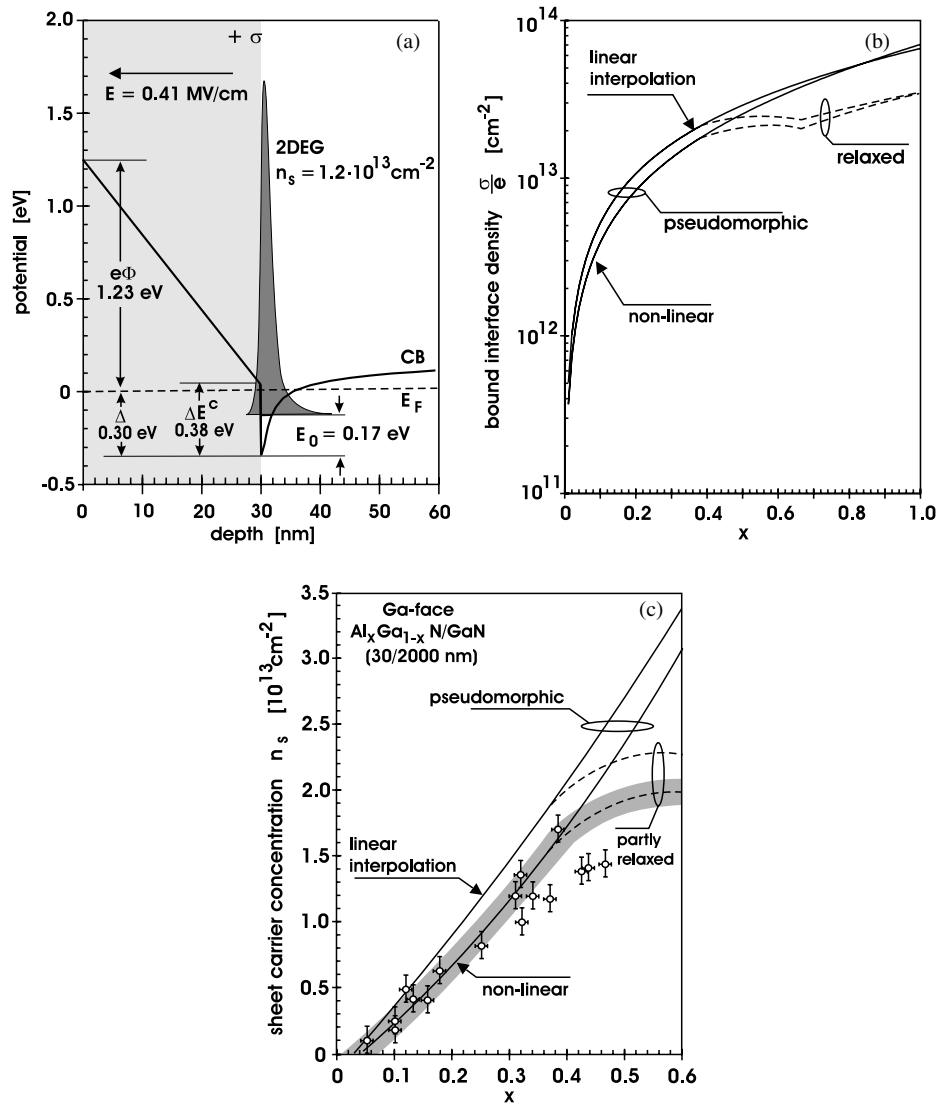


Figure 12. (a) Self-consistent calculation of the conduction band and electron concentration profile of an undoped Ga-face Al_{0.3}Ga_{0.7}N/GaN (30/2000 nm) heterostructure including the Schottky barrier of the Ni contact on top and the polarization-induced surface and interface charges. (b) The polarization-induced bound interface sheet densities are shown as a function of alloy composition of the barrier for Ga-face AlGa_xN/GaN heterostructures. The sheet density is calculated for barriers grown on relaxed GaN using again (i) a linear interpolation of the physical properties (C_{ij} , e_{ij} and P^{SP}) of the binary compounds (upper solid curve) and (ii) considering the nonlinear behaviour of piezoelectric and spontaneous polarization (lower solid curve). The dashed curves show the change of the sheet density with increasing x taking the measured degree of barrier relaxation into account. (c) The 2DEG sheet carrier concentrations are shown as a function of alloy composition of the barrier for Ga-face AlGa_xN/GaN heterostructures (30/2000 nm). The sheet carrier concentration is calculated for barriers grown on relaxed GaN using again (i) a linear interpolation (upper solid curve) and (ii) considering the nonlinear behaviour of piezoelectric and spontaneous polarization (lower solid curve). The grey area along this curve indicates the uncertainty (which is very similar for the linear and nonlinear approaches) in the calculated values of n_s . The measured 2DEG carrier concentrations obtained by C - V -profiling are shown as open symbols. The dashed curves show the further increase of the sheet carrier concentration with increasing x for AlGa_xN/GaN heterostructures, taking the measured degree of barrier relaxation into account [25].

We used the following linear interpolations to describe the physical properties of the alloys in our calculations (values for InGaN are given for completeness and further calculations). Dielectric constants [59]:

$$\begin{aligned} \varepsilon_{\text{AlGaN}}(x) &= 0.03x + 10.28 \\ \varepsilon_{\text{InGaN}}(x) &= 4.33x + 10.28 \\ \varepsilon_{\text{AlInN}}(x) &= -4.30x + 14.61. \end{aligned} \quad (54)$$

Schottky barrier for Ni contact [60]:

$$\begin{aligned} e\phi_{\text{AlGaN}}(x) &= (1.3x + 0.84) \text{ eV} \\ e\phi_{\text{InGaN}}(x) &= (-0.36x + 0.84) \text{ eV} \\ e\phi_{\text{AlInN}}(x) &= (1.66x + 0.48) \text{ eV}. \end{aligned} \quad (55)$$

Bandgaps [38, 61–63]:

$$\begin{aligned} E_{\text{AlGaN}}^g(x) &= [6.13x + 3.42(1-x) - 1.0x(1-x)] \text{ eV} \\ E_{\text{InGaN}}^g(x) &= [1.95x + 3.42(1-x) - 2.5x(1-x)] \text{ eV} \\ E_{\text{AlInN}}^g(x) &= [6.13x + 1.95(1-x) - 5.4x(1-x)] \text{ eV}. \end{aligned} \quad (56)$$

Band offsets [64, 65]:

$$\Delta E_{\text{ABN}}^C(x) = 0.63(E_{\text{ABN}}^g(x) - E_{\text{ABN}}^g(0)) \quad (57)$$

and an electron effective mass of $m_{\text{GaN}}^* = 0.228 m_0$ for GaN [66].

In order to determine the sheet carrier concentrations and carrier distribution profiles in undoped HEMT structures including spontaneous and piezoelectric polarization-induced bound sheet charges, and to verify the results obtained with the equations above, we have used a one-dimensional Schrödinger–Poisson solver [67]. To incorporate the effects of the nonlinear spontaneous and piezoelectric polarization into the program, thin ($\approx 6 \text{ \AA}$) layers of charge are added to the heterostructure interfaces to simulate the bound sheet density σ/e .

For both kinds of calculation it is necessary to specify the boundary conditions at the surface and at the substrate interfaces. In our HEMT structures we have assumed a Ni Schottky barrier contact at the surface, which pins the conduction band according to equation (55). At the interface to the substrate, the Fermi level was set to the mid-gap of GaN. Changing this value of the Fermi level has very little impact on the sheet carrier concentration of the 2DEG for GaN buffer thicknesses above $1 \mu\text{m}$. For the same boundary conditions the calculations of the 2DEG sheet carrier concentrations using equation (51) or the Schrödinger–Poisson solver agree within 5% for all HEMT structures investigated.

(i) 2DEGs confined at interfaces of undoped Ga-face AlGaN/GaN heterostructures. In typical undoped AlGaN/GaN HEMTs with insulating buffers ($N_d < 10^{16} \text{ cm}^{-3}$), GaN thicknesses of about $2 \mu\text{m}$ and barrier widths of more than 15 nm, the value of the sheet carrier concentration is dominated by the polarization-induced sheet charge. This charge increases with increasing Al concentration in the barrier, because the strain and, therefore, the piezoelectric polarization as well as the spontaneous polarization are increasing. This offers the possibility to control the sheet carrier concentration of the 2DEG by the choice of the Al concentration of the barrier instead of barrier doping. In figure 12(a) the conduction band and electron concentration profiles are shown for an undoped Ga-face $\text{Al}_{0.3}\text{Ga}_{0.7}\text{N}/\text{GaN}$ (30/2000 nm) heterostructure with a Ni Schottky contact on top. The polarization-induced surface and interface charges cause an electric field of about 0.4 MV cm^{-1} inside the barrier and an accumulation of electrons with a sheet carrier concentration of $1.2 \times 10^{13} \text{ cm}^{-2}$ at the AlGaN/GaN interface. In figures 12(b) and (c) the polarization-induced bound sheet densities and 2DEG sheet carrier concentrations

are shown for heterostructures with the same design but different alloy compositions of the barrier. The bound interface sheet density is calculated for barriers grown on relaxed GaN (i) using again a linear interpolation of the physical properties (C_{ij} , e_{ij} and P^{SP}) of the binary compounds (upper solid curve) and (ii) considering the nonlinear behaviour of piezoelectric and spontaneous polarization (lower solid curve). The grey area in figure 12(c) along one of the curves indicates the uncertainty (which is very similar for the linear and nonlinear approaches) in the calculated values of n_s , which is mainly caused by the error in the determination of the barrier thickness and the conduction band offsets. To enable a comparison between experimental (open symbols) and theoretical data, the sheet carrier concentration of the 2DEGs is calculated as described above, taking into account the depletion caused by the Ni Schottky contact (figure 12(c)). Experimentally, the sheet carrier concentrations of 2DEGs confined in AlGaIn/GaN heterostructures with alloy compositions of up to $x = 0.5$ are measured by $C-V$ -profiling using Ti/Al ohmic and Ni Schottky contacts. The highest measured and calculated sheet carrier concentration for pseudomorphic AlGaIn/GaN heterostructures is determined to be $2 \times 10^{13} \text{ cm}^{-2}$ for $x = 0.37$. For higher Al concentration, the AlGaIn barrier starts to relax, diminishing the piezoelectric component [25]. The dashed extrapolations in figures 12(b) and (c) show the further variation of the sheet carrier concentration with increasing x , taking the measured degree of relaxation of the barrier into account. For lower Al concentrations of the 30 nm thick barriers the sheet carrier concentration decreases nonlinearly down to $x \approx 0.06$, where the 2DEG disappears.

For pseudomorphic HEMT structures with barrier thicknesses of more than 15 nm, the nonlinear dependence of the 2DEG carrier concentration on the alloy composition can be approximated very well by

$$n_s(x) = [-0.169 + 2.61x + 4.50x^2]10^{13} \text{ cm}^{-2} \quad x > 0.06. \quad (58)$$

For thinner barriers the depletion by the Schottky contact or the influence of the surface charge of the heterostructure becomes important (for more information see [58]). In figure 13, the dependence of $n_s(x)$ on the AlGaIn barrier thickness according to equation (51) for $x = 0.15$, 0.30 and 0.45 is shown. A drastic decrease in sheet carrier concentration is predicted for thicknesses below 12, 8 and 6 nm, respectively. For $x = 0.3$ the sheet carrier concentration of AlGaIn/GaN HEMTs was measured by $C-V$ -profiling for barrier thicknesses between 1 and 50 nm. These data and experimental results of other groups are presented by the data points in figure 13 [68, 69]. A reasonable agreement between our theoretical predictions and the experimental data is found.

A comparison of the calculated bound sheet charge and the 2DEG sheet carrier concentration with the measured interface-accumulated free charge is clearly more direct than if it is compared with the Stark shift of excitonic radiative recombinations due to the depolarizing field as discussed later. More important, the nonlinear prediction reproduces the measured data accurately, recovering almost all of the residual deviations from experiment observed in former approaches [6, 70, 71]. The predicted piezoelectric and spontaneous polarization therefore can be considered as fairly reliable for AlGaIn/GaN heterostructures.

(ii) 2DEGs confined at interfaces of undoped Ga-face AlInN/GaN heterostructures. In order to determine the precise composition x and the strain of AlInN barriers grown on Ga-face buffer layers, reciprocal space maps of the symmetric (200) and asymmetric (205) reflexes were measured by HRXRD. From the reciprocal space maps (figure 14) it can be seen that the $\text{Al}_x\text{In}_{1-x}\text{N}/\text{GaN}$ (50/540 nm) heterostructures with Al concentrations between 0.78 and 0.88 are grown pseudomorphically. The GaN buffer layer is under weak compressive strain ($\varepsilon_1 = -1.9 \times 10^{-3}$), causing a piezoelectric polarization of 0.0015 C m^{-2} . More important, by

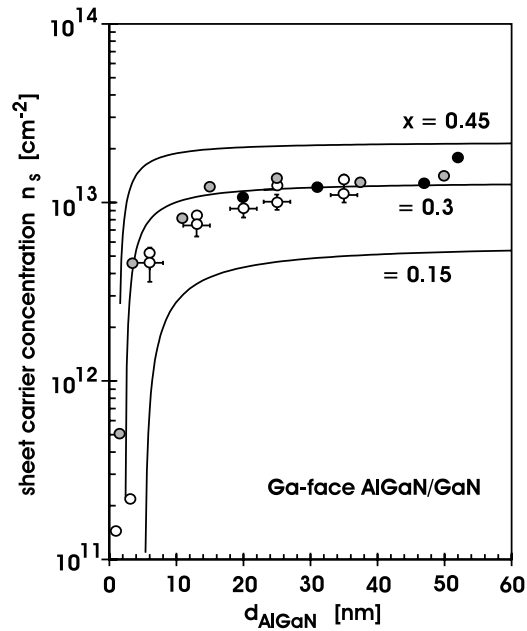


Figure 13. The dependences of $n_s(x)$ on barrier thickness calculated using equation (51) for $x = 0.15, 0.30$ and 0.45 are shown. A drastic decrease in sheet carrier concentration is predicted for thicknesses below 12, 8 and 6 nm, respectively. For $x = 0.3$ the sheet carrier concentration of AlGaIn/GaN HEMTs was measured by C - V -profiling for barrier thicknesses between 1 and 50 nm. These data (white open symbols) and experimental results of other groups (black and grey symbols [68,69]) are in good agreement with the theoretical predictions.

calculating the strain of the AlInN along the c -axis and in the basal plane using the measured lattice constants, the Al concentration at which AlInN can be grown lattice matched to the GaN buffer layer is determined to be $x = (0.83 \pm 0.01)$ (figure 15). Close to this composition the piezoelectric polarization in the AlInN layer vanishes. Although the AlInN barrier is not intentionally doped and the residual piezoelectric polarization of the insulating GaN buffer layer can cause a maximum, negative bound sheet density of only $-\frac{\sigma}{e} \approx -10^{12} \text{ cm}^{-2}$, sheet carrier concentrations of accumulated electrons of more than 10^{13} cm^{-2} are measured by the Hall effect and C - V -profiling (figure 16). In figure 17 the bound sheet density caused by the gradient in piezoelectric (lower solid line) and spontaneous polarization (upper dashed line) as well as the calculated 2DEG sheet carrier concentration (upper solid line) are shown. It is obvious that the calculated positive bound sheet density and the measured 2DEG sheet carrier concentrations of the lattice-matched heterostructures can only be caused by a gradient in spontaneous polarization at the AlInN/GaN interface. The observation of high concentrations of accumulated electrons in these samples provides direct evidence for the presence of a strong gradient in spontaneous polarization at the heterostructure interface. The predicted sheet carrier concentrations for lattice-matched AlInN/GaN heterostructures obtained by a linear interpolation of the physical properties (C_{ij} , e_{ij} and P^{SP}) of the binary compounds and taking the nonlinearity of P^{Pz} and P^{SP} into account are $n_s(0.82) = 2.95 \times 10^{13}$ and $2.28 \times 10^{13} \text{ cm}^{-2}$, respectively. Again, our improved nonlinear theory agrees better with the measured sheet carrier concentration of about $(1.5 \pm 0.1) \times 10^{13} \text{ cm}^{-2}$. The relatively large discrepancy between the measured and calculated values for n_s could be caused by an underestimation of the bowing parameters used to describe the nonlinearity of P^{Pz} and P^{SP} , but

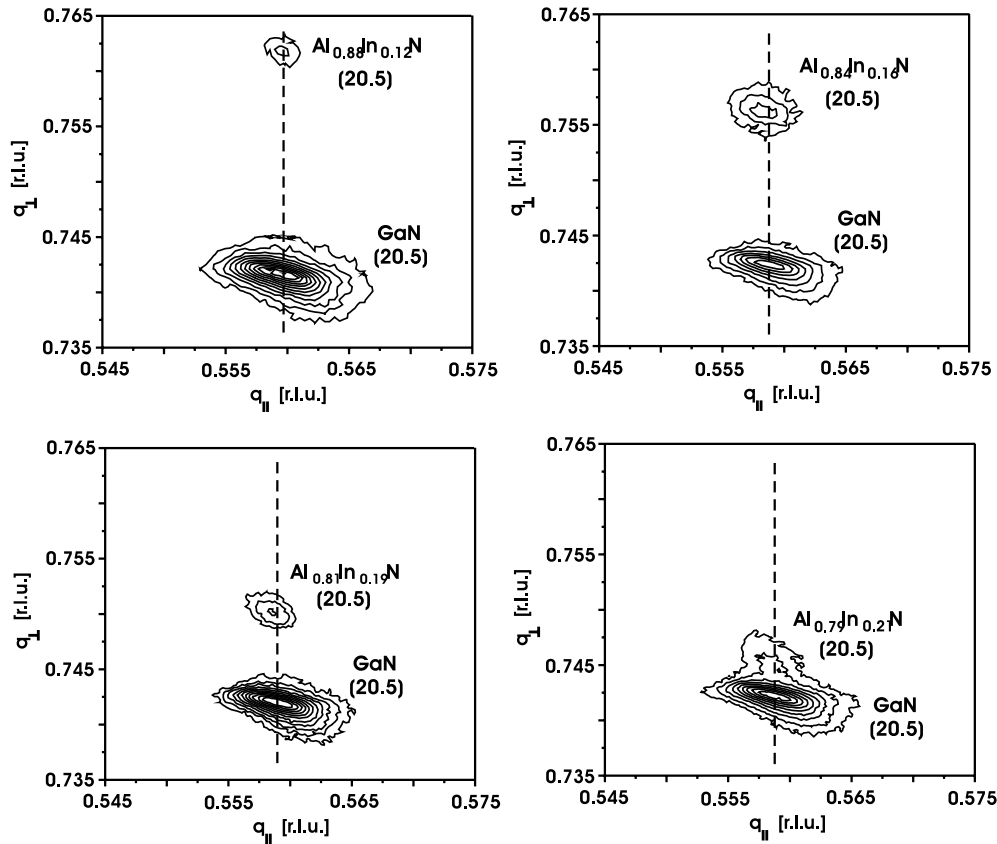


Figure 14. Reciprocal space maps of the (20.5) reflections of undoped AlInN/GaN heterostructures measured by HRXRD. AlInN barriers with Al concentrations between $x = 0.79$ and 0.88 are grown pseudomorphically.

more likely charged defects located close to the AlInN/GaN interface and/or charged adsorbates at the free surface screen part of the bound polarization-induced interface charge, thus lowering the measured concentration of free electrons. Also In fluctuations causing a smearing and reduction of the polarization-induced interface charge can be present in the AlInN barriers. A further improvement in the agreement between experimental and theoretical results can be expected if the structural and interface quality of the heterostructures are optimized.

(iii) *2DEGs confined in a single InGaN/GaN QW.* Single InGaN/GaN QWs offer two additional possibilities to obtain information about polarization-induced interface charges. First, in analogy to the AlGaIn/GaN and AlInN/GaN HEMT structures, the formation of 2DEGs in InGaN SQWs can be measured. Second, the Stark shift of excitonic recombination can be used to determine the polarization-induced electric field inside the QW and the polarization-induced bound charge located at the InGaN/GaN interfaces.

We have investigated nominally undoped, n-type GaN/In_{0.13}Ga_{0.87}N/GaN nanostructures with Ga-face polarity, where the width of the pseudomorphic SQW was varied between $d_{\text{InGaN}} = 0.9$ and 54 nm [48, 49]. The spontaneous polarization of the InGaN layer ($P_{\text{InGaN}}^{\text{SP}}(x = 0.13) = -0.031$ C m⁻²), pointing in the $[000\bar{1}]$ -direction, is predicted to be

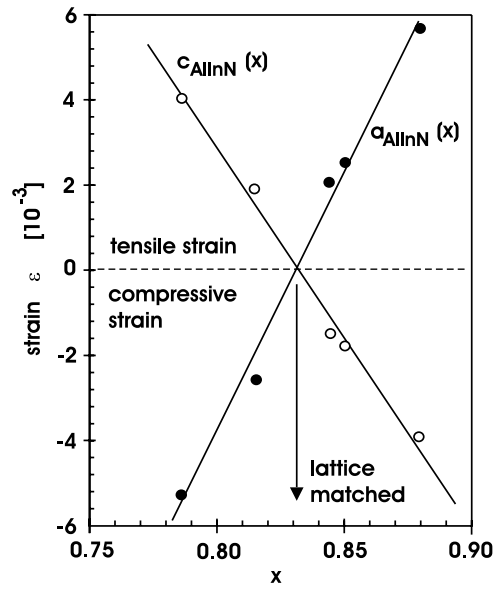


Figure 15. Strain of the AlInN barrier along the c -axis and in the basal plane, determined from the measured lattice constants $c_{\text{AlInN}}(x)$ and $a_{\text{AlInN}}(x)$. For $x = 0.83$ the pseudomorphic AlInN layer is grown lattice matched on the GaN buffer layer.

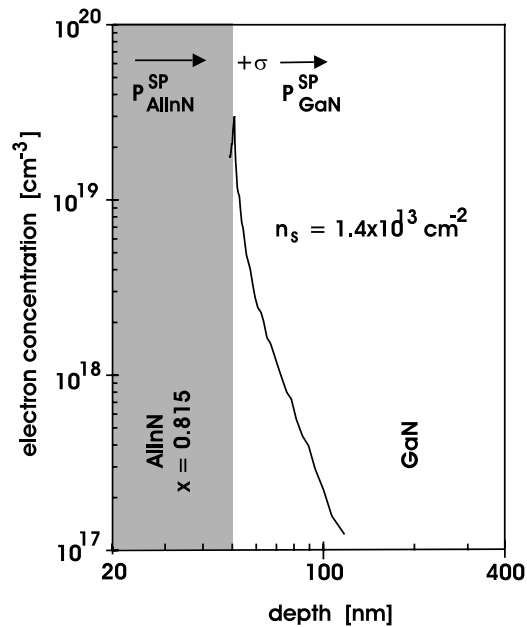


Figure 16. Electron concentration profile measured by C - V -profiling of a nearly lattice-matched AlInN/GaN heterostructure (50/540 nm) with Ga-face polarity. A very high concentration of electrons accumulated at the AlInN/GaN interface is obtained.

slightly smaller than the polarization of the relaxed GaN buffer and cap layer. The piezoelectric polarization is calculated to be $P_{\text{InGaN}}^{\text{PZ}}(x = 0.13) = 0.016 \text{ C m}^{-2}$. Because the InGaN well is under compressive strain, the piezoelectric polarization is anti-parallel to $P_{\text{InGaN}}^{\text{SP}}$. The gradient

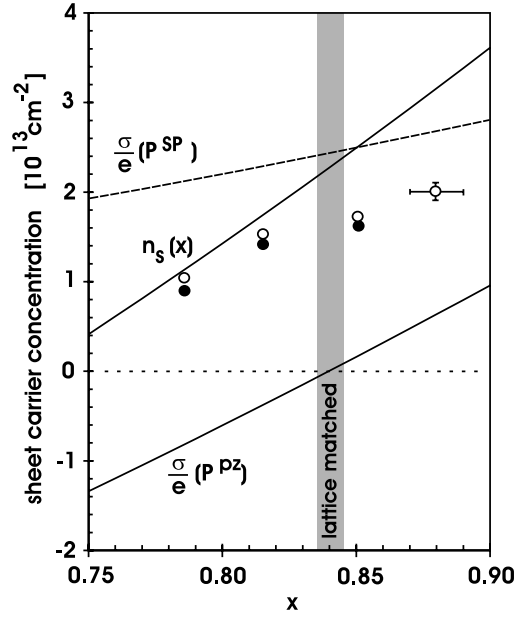


Figure 17. Calculated bound sheet densities located at $\text{Al}_x\text{In}_{1-x}\text{N}/\text{GaN}$ interfaces, induced by a gradient in piezoelectric polarization (lower solid line) and/or a gradient in spontaneous polarization (dashed line) in dependence on Al concentration of the barrier. The predicted 2DEG sheet carrier concentration (upper solid line) is compared with concentrations determined by Hall effect (solid symbols) and C - V -profiling (open symbols) measurements. For lattice-matched heterostructures (grey area) sheet carrier concentrations of more than 10^{13} cm^{-2} are predicted and measured, proving the presence of a large gradient in spontaneous polarization at the heterostructure interface.

in total polarization at the InGaN/GaN interface should cause a polarization-induced interface sheet density of

$$\begin{aligned} \frac{\sigma}{e} &= \frac{1}{e} \left\{ (P_{\text{GaN}}^{\text{SP}} + P_{\text{GaN}}^{\text{PZ}}) - (P_{\text{InGaN}}^{\text{SP}} + P_{\text{InGaN}}^{\text{PZ}}) \right\} \\ &= \frac{1}{e} \{ (-0.034 + 0) - (-0.031 + 0.016) \} \text{ C m}^{-2} = 1.18 \times 10^{13} \text{ cm}^{-2}. \end{aligned} \quad (59)$$

It should be mentioned that the bound polarization-induced charge in these heterostructures is positive at the interface close to the surface, whereas the lower interface of the InGaN QW is negatively charged. Therefore, in analogy to the AlGaIn/GaN and AlInN/GaN heterostructures, the formation of a 2DEG is expected at the upper interface. In the heterostructures examined here, 2DEGs with sheet carrier concentrations equal to the bound interface charge should be observed 130 nm below the surface for wells with widths of more than 20 nm. Measured C - V -profiles of the carrier concentration of the nanostructures are shown in figure 18. For well widths above 4 nm an accumulation of electrons can be confirmed. By increasing the thickness of the InGaIn QWs from 4.3 to 54 nm, the sheet carrier concentration increases from $n_s = 3.6 \times 10^{10}$ to $5 \times 10^{12} \text{ cm}^{-2}$ (figure 19). The increase in 2DEG sheet carrier concentration is much faster than the increase of the volume of the InGaIn layer ($n_s \propto d^{2.5}$). This can be partly caused by the reduction of the effective ionization energy of donors inside the well due to the strong polarization-induced electric field. However, even for thick InGaIn SQWs the measured electron density of the 2DEGs is below 50% of the predicted bound interface charge.

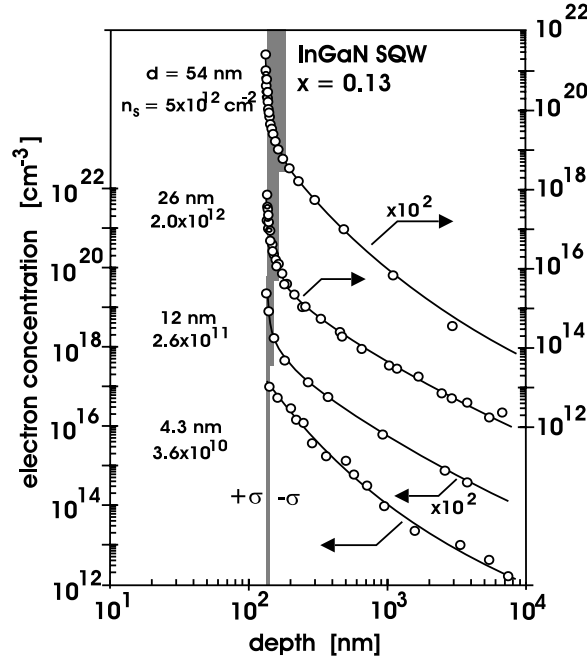


Figure 18. Electron concentration profiles measured by *C*–*V*-profiling of undoped, n-type GaN/In_{0.13}Ga_{0.87}N/GaN QWs with well widths of 4.3, 12, 26 and 54 nm, respectively. For comparison the carrier profiles are shifted against each other. For QWs (grey area) with widths of more than 4.3 nm, the formation of 2DEGs at the upper interface, compensating part of the positive polarization-induced charge, can be confirmed.

This raises the question of whether the polarization-induced interface charges in InGaN/GaN SQWs are not completely screened by electrons and ionized donors. In this case, an electric field causing a red shift of the radiative recombination of excitons should be present in the InGaN QW, scaling with the thickness of the well. Assuming that the polarization-induced charges at the free surface and at the GaN/substrate interface are completely screened by adsorbed charge from the ambient or charged interface defects (which is in agreement with our experiments discussed in [56]), the electric field inside an insulating well can be calculated by

$$E_{\text{InGaN}} = -\frac{1}{\varepsilon_0 (\varepsilon_{\text{InGaN}} - 1)} \{ (P_{\text{GaN}}^{\text{SP}} + P_{\text{GaN}}^{\text{PZ}}) - (P_{\text{InGaN}}^{\text{SP}} + P_{\text{InGaN}}^{\text{PZ}}) \}. \quad (60)$$

If free carriers confined in the well are not homogeneously distributed, as is the case in the presence of a 2DEG, the slope of the conduction band edge and the electric field inside the InGaN are not constant (for more detailed information see [72]). In this case the average electric field can be approximated by

$$\overline{E}_{\text{InGaN}} = -\frac{e}{\varepsilon_0 (\varepsilon_{\text{InGaN}} - 1)} \left\{ \frac{\sigma}{e} - n_s \right\}. \quad (61)$$

For In_{0.13}Ga_{0.87}N QWs with well widths below 6 nm the screening by free carriers can be neglected and a very high electric field of 2.2 MV cm⁻¹ is predicted by equation (60). For the thickest QW of 54 nm, the observed 2DEG should only partially screen the predicted interface charge, leaving an average field of about 1.3 MV cm⁻¹.

In the presence of an electric field and in the absence of free carriers, the rectangular usual shape of a QW has to be replaced by a triangular shape (figure 20), in which the energy of the

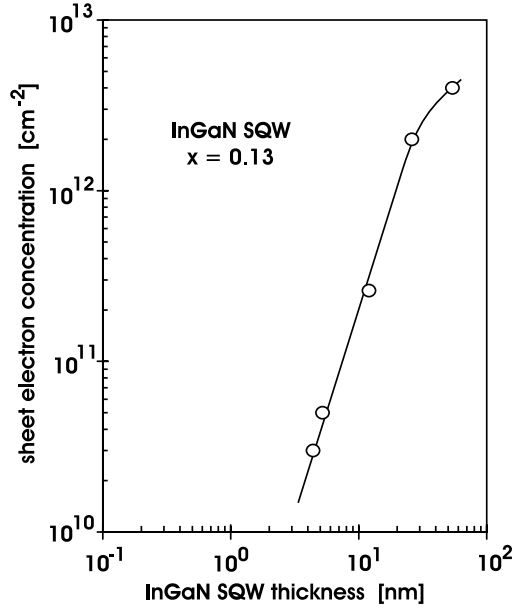


Figure 19. The increase of sheet carrier concentration inside the InGaN layers in dependence on the widths of the QWs.

radiative recombination between the hole and electron ground level is described by

$$E_{0e0h} = E_{\text{InGaN}}^g - eE_{\text{InGaN}}d_{\text{InGaN}} + \left(\frac{9\pi\eta e E_{\text{InGaN}}}{8\sqrt{2}} \right)^{2/3} \left(\frac{1}{m_{\text{InGaN},e}^*} + \frac{1}{m_{\text{InGaN},h}^*} \right)^{1/3} \quad (62)$$

where $m_{\text{InGaN},e}^* \approx m_{\text{GaN},e}^* = 0.228m_0$ and $m_{\text{InGaN},h}^* \approx m_{\text{GaN},h}^* = 0.9m_0$ are the effective electron and hole masses of InGaN, respectively, which we approximated by the effective masses of GaN [73]. The energy of the radiative recombination E_{0e0h} and the bandgap of the InGaN QW as a function of the well width have been measured earlier using the same samples by Ramakrishan *et al* [49]. The bandgap is determined by spectroscopic ellipsometry and room-temperature PL using an excitation energy of 3.41 eV, only absorbed by the InGaN well. The QW is pumped with high intensity in order to generate a high density of electron–hole pairs, completely screening the polarization-induced electric field. The Stark shift is measured also by PL, but using the lowest possible pumping power and a photon energy of 3.81 eV, well above the bandgap of GaN. Using this experimental procedure, the screening of the polarization-induced charge by photogenerated carriers is negligible.

For $\text{In}_{0.13}\text{Ga}_{0.87}\text{N}$ QWs with widths of more than 26 nm we have measured a bandgap of (2.902 ± 0.012) eV, in good agreement with the value for bulk InGaN of the same composition ($E_{\text{InGaN}}^g(x = 0.13) = 2.946$ eV). The spectroscopic ellipsometry and PL data recorded with direct QW excitation at 3.41 eV show a monotonic shift to higher energies, reaching a value of 3.21 eV if the well width is decreased to 0.9 nm, as expected for pure quantum confinement (figure 21). PL spectra measured by excitation at 3.81 eV with a pumping power density of 1 kW cm^{-2} yield a PL peak position which is increasingly shifted to lower energies if the QW width is increased from 0.9 to 5.3 nm (Stark effect). From this measured red shift of the PL peak position and equation (62), an electric field strength of 0.83 MV cm^{-1} can be estimated for thin QWs. This field strength corresponds to an unscreened polarization-induced bound interface density of about $\frac{\sigma}{e} = 5 \times 10^{12} \text{ cm}^{-2}$. The measured electric field and

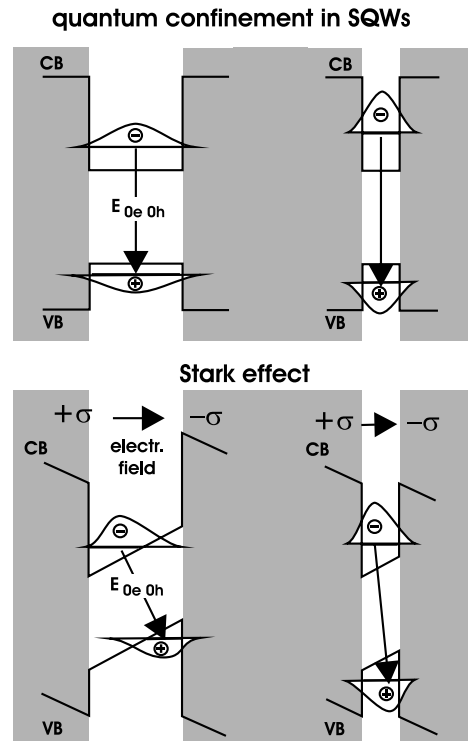


Figure 20. Schematic drawing of the band edge profiles of two QWs with different thicknesses. The radiative recombination between the hole and electron ground levels inside the rectangular QW is increasing in energy with decreasing well width due to quantum confinement. The optical transition is blue shifted. In the presence of a polarization-induced electric field, the shape of the rectangular well has to be replaced by a triangular QW in which the recombination of the photogenerated electron–hole pairs is red shifted due to the Stark effect.

calculated interface charges are in good agreement with the data obtained by Wetzel *et al* [74] for $\text{In}_{0.12}\text{Ga}_{0.88}\text{N}/\text{GaN}$ MQWs of 0.62 MV cm^{-1} , corresponding to $\frac{\sigma}{e} = 3.7 \times 10^{12} \text{ cm}^{-2}$.

The polarization-induced charge deduced from the measured red shift fits very well our experimental observation, namely that the Stark shift is not detectable for QWs with a width of more than 26 nm (figure 21). For these samples, the measured bandgap of InGaN and the PL peak position agree within 40 meV. Especially for the thickest QW it is obvious that the polarization-induced interface charge must be completely screened by the presence of a 2DEG (figure 18) with a sheet carrier concentration of $5 \times 10^{12} \text{ cm}^{-2}$. Both the measured Stark shift and the 2DEG sheet carrier density indicate an unscreened bound interface charge of $5 \times 10^{12} \text{ cm}^{-2}$ located at $\text{In}_{0.13}\text{Ga}_{0.87}\text{N}/\text{GaN}$ interfaces. A significant discrepancy of about 50% is observed between the predicted and measured polarization-induced sheet charge in the case of InGaN/GaN heterostructures. Our data prove that this discrepancy is not caused by screening due to free carriers.

What are possible explanations for the deviation of our theory from the experimental data in the case of InGaN/GaN heterostructures? One reason for the measured low polarization-induced interface charge could be the presence of indium fluctuations, which were observed on a scale of about 10 nm inside thick wells. Indium fluctuations will smear out the polarization-induced charge throughout the well, causing a complex profile of the electric

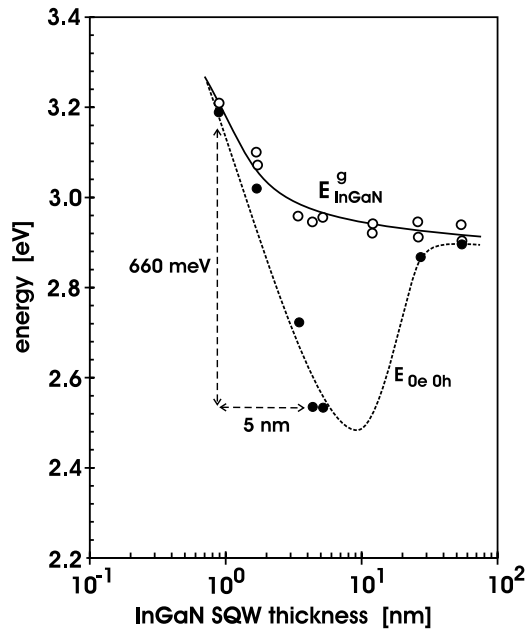


Figure 21. The bandgap of the $\text{In}_{0.13}\text{Ga}_{0.87}\text{N}$ QWs and the energy of the radiative recombination in dependence on the well width. The bandgap is determined by spectroscopic ellipsometry and room-temperature PL using an excitation energy of 3.41 eV, only absorbed by the InGaN well. The QW is pumped with high intensity in order to generate a high density of electron-hole pairs, completely screening the polarization-induced electric field. The Stark shift is also measured by PL, but using the lowest possible pumping power and a photon energy of 3.81 eV, well above the bandgap of GaN [49]. By this experimental procedure the screening of the polarization-induced charge by photogenerated carriers is negligible.

field. These effects are not included in our one-dimensional model of polarization-induced effects. Another explanation could be the presence of charged, fixed point defects caused by impurities, vacancies or charged structural defects, located at grain boundaries and screening the polarization-induced charge but not showing up in our electronic characterization.

The influence of In fluctuations can be understood by simulating the corresponding strain fields and piezoelectric polarization profiles in a two-dimensional theory, combining finite-element and tight-binding calculations. Information on charged defects in InGaN can be obtained by a combination of temperature-dependent Hall measurements and deep-level transient spectroscopy. Both approaches are under progress in order to improve our understanding of polarization-induced effects in InGaN/GaN-based nanostructures relevant for LED and laser applications.

9. Summary

We have presented theoretical and experimental evidence for the nonlinearity of spontaneous and piezoelectric polarization in nitride alloys as a function of strain and composition. We have applied our improved theory to reverse-model experimental data obtained from a number of InGaN/GaN QW as well as AlInN/GaN and AlGaIn/GaN transistor structures. We have found that the discrepancies of experiment and *ab initio* theory so far present in the literature are almost completely eliminated for the AlGaIn/GaN-based heterostructures when polarization

nonlinearity is taken into account. To facilitate inclusion of the predicted nonlinear polarization in future simulations, we have given an explicit prescription to calculate polarization-induced surface and interface charges as well as electric fields for arbitrary compositions in each of the random ternary III–N alloys.

With the realization of undoped lattice-matched AlInN/GaN heterostructures we were able to prove the existence of a gradient in spontaneous polarization predicted by theory. The confinement of 2DEGs in InGaN/GaN QWs in combination with the measured Stark shift of excitonic recombinations was used to determine the polarization-induced electric fields and interface charges. A significant discrepancy between the predicted and measured bound interface charges is found, motivating the development of a two-dimensional model for polarization-induced effects in QWs with In fluctuations and a more detailed characterization of charged defects in the future.

Acknowledgments

The authors would like to thank J Wagner (Fraunhofer Institute, Freiburg, Germany) as well as J Off and F Scholz (University of Stuttgart, Germany) for providing high-quality InGaN/GaN and AlInN/GaN heterostructures. The work was partly supported by the Deutsche Forschungsgemeinschaft (Stu 139/2). The calculations performed at Cagliari University were supported in part by MURST, Cofin99 and the INFN Parallel Supercomputing Initiative. The experiments performed at Cornell University are supported by the Office of Naval Research under the direction of Dr C Wood.

References

- [1] Bernardini F, Fiorentini V and Vanderbilt D 1997 *Phys. Rev. B* **56** R10 024
- [2] Zoroddu A, Bernardini F, Ruggerone P and Fiorentini V 2001 *Phys. Rev. B* **64** 45 208
- [3] Ambacher O 1998 *J. Phys. D: Appl. Phys.* **31** 2653
- [4] Dubois M-A and Muralet P 1999 *Appl. Phys. Lett.* **74** 3032
- [5] Dimitrov R, Mitchell A, Wittmer L, Ambacher O, Stutzmann M, Hilsenbeck J and Rieger W 1999 *Japan. J. Appl. Phys.* **38** 4962
- [6] Ambacher O *et al* 1999 *J. Appl. Phys.* **85** 3222
- [7] Shur M S, Bykhovski A D and Gaska R 1999 *Mater. Res. Soc. Int. J. Nitr. Semicond. Res. S* **41** G16
- [8] Tsubouchi K and Mikoshiba N 1983 *IEEE Ultrason. Symp.* **90** 299
- [9] Palacios T, Calle F, Monroy E, Grajal J, Eickhoff M, Ambacher O and Prieto C 2001 *Proc. E-MRS Meeting, Symp. H Paper H/PI.17*
- [10] Deger C, Born E, Angerer H, Ambacher O, Stutzmann M, Hornsteiner J, Riha E and Fischerauer G 1998 *Appl. Phys. Lett.* **72** 2400
- [11] Tsubouchi K, Sugai K and Mikoshiba N 1981 *IEEE Ultrason. Symp.* **90** 375
- [12] Wetzel C, Takeuchi T, Yamaguchi S, Katoh H, Amano H and Akasaki I 1998 *Appl. Phys. Lett.* **73** 1994
- [13] Im J S, Härle V, Scholz F and Hangleiter A 1996 *Mater. Res. Soc. Int. J. Nitr. Semicond. Res.* **1** 37
- [14] Grandjean N, Massies J and Leroux M 1999 *Appl. Phys. Lett.* **74** 2361
- [15] Nakamura S and Fasol G 1998 *The Blue Laser Diode—GaN Based Light Emitters and Lasers* (Berlin: Springer)
- [16] Nakamura S 1999 *Semicond. Sci. Technol.* **14** R27
- [17] Eastman L F *et al* 2001 *IEEE Trans. Electron Devices* **48** 479
- [18] Ozgur A, Kim W, Fan Z, Botchkarev A, Salvador A, Mohammad S N, Sverdlov B and Morkoc H 1995 *Electron. Lett.* **31** 1389
- [19] Khan M A, Chen Q, Shur M S, MsDermott B T, Higgins J A, Burm J, Schaff W J and Eastman L F 1996 *IEEE Electron Device Lett.* **17** 584
- [20] Binari S C, Redwing J M, Kelner G and Kruppa W 1997 *Electron. Lett.* **33** 242
- [21] Gaska R, Chen Q, Yang J, Osinsky A, Khan M A and Shur M S 1997 *IEEE Electron Device Lett.* **18** 492
- [22] Wu Y F, Keller S, Kozodoy P, Keller B P, Parikh P, Kapolnek D, DenBaars S P and Mishra U K 1997 *IEEE Electron Device Lett.* **18** 290

- [23] Dimitrov R, Wittmer L, Felsl H P, Mitchell A, Ambacher O and Stutzmann M 1998 *Phys. Status Solidi a* **168** R7
- [24] Eastman L F *et al* 2001 *Proc. 28th Int. Symp. on Compound Semiconductors, ISCS 2001 (Tokyo)*
- [25] Ambacher O *et al* 2000 *J. Appl. Phys.* **87** 334
- [26] Kresse G and Hafner J 1993 *Phys. Rev. B* **47** 558
- [27] Kresse G and Furthmüller J 1996 *Comput. Mater. Sci.* **6** 15
- [28] King-Smith R D and Vanderbilt D 1993 *Phys. Rev. B* **47** 1651
- [29] Resta R 1994 *Rev. Mod. Phys.* **66** 899
- [30] Perdew J P 1991 *Electronic Structure of Solids '91* ed P Ziesche and H Eschrig (Berlin: Akademie) p 11
- [31] Wei S-H, Ferreira L G, Bernard J E and Zunger A 1990 *Phys. Rev. B* **42** 9622
- [32] Görgens L, Ambacher O, Stutzmann M, Miskys C, Scholz F and Off J 2000 *Appl. Phys. Lett.* **76** 577
- [33] Angerer H *et al* 1997 *Appl. Phys. Lett.* **71** 1504
- [34] Peng T, Piprek J, Qiu G, Olowolafe J O, Unruh K M, Swann C P and Schubert E F 1997 *Appl. Phys. Lett.* **71** 2439
- [35] Bellaiche L, Wei S-H and Zunger A 1997 *Phys. Rev. B* **56** 13 872
- [36] Mattila T and Zunger A 1999 *J. Appl. Phys.* **85** 160
- [37] O'Donnell K P, Mosselmanns J F W, Martin R W, Pereira S and White M E 2001 *J. Phys.: Condens. Matter* **13** 6977
- [38] Bernardini F and Fiorentini V 2001 *Phys. Rev. B* **64** 85 207
- [39] Hellman E S 1998 *Mater. Res. Soc. Int. J. Nitr. Semicond. Res.* **3** 11
- [40] Daudin B, Rouvière J L and Arley M 1996 *Appl. Phys. Lett.* **69** 2480
- [41] Seelmann-Eggebert M, Weyher J L, Obloh H, Zimmermann H, Rar A and Porowski S 1997 *Appl. Phys. Lett.* **71** 2635
- [42] Smith A R, Feenstra R M, Greve D W, Neugebauer J and Northrup J E 1997 *Phys. Rev. Lett.* **79** 3934
- [43] Smith A R, Feenstra R M, Greve D W, Shin M S, Skowronski M, Neugebauer J and Northrup J E 1998 *Appl. Phys. Lett.* **72** 2114
- [44] Batterman B W 1969 *Phys. Rev. Lett.* **22** 703
- [45] Kazimirov A, Scherb G, Zegenhagen J, Lee T-L, Bedzyk M J, Kelly M K, Angerer H and Ambacher O 1998 *J. Appl. Phys.* **84** 1703
- [46] Smart J A, Schremer A T, Weimann N G, Ambacher O, Eastman L F and Shealy J R 1999 *Appl. Phys. Lett.* **75** 388
- [47] Murphy M J, Chu K, Wu H, Yeo W, Schaff W J, Ambacher O, Smart J, Shealy J R, Eastman L F and Eustis T J 1999 *J. Vac. Sci. Technol. B* **17** 1252
- [48] Wagner J, Ramakrishnan A, Obloh H and Maier M 1999 *Appl. Phys. Lett.* **74** 3863
- [49] Ramakrishnan A, Wagner J, Kunzer M, Obloh H, Köhler K and Johs B 2000 *Appl. Phys. Lett.* **76** 79
- [50] Kasic A, Schubert M, Off J and Scholz F 2001 *Appl. Phys. Lett.* **78** 1526
- [51] Wright A F 1997 *J. Appl. Phys.* **82** 2833
- [52] O'Clock G D and Duffy M T 1973 *Appl. Phys. Lett.* **23** 55
- [53] Nye J F 1985 *Physical Properties of Crystals; Their Representation by Tensors and Matrices* (Oxford: Clarendon)
- [54] Jogai B 2001 *J. Appl. Phys.* **90** 699
- [55] Rotter M, Wixforth A, Govorov A O, Ruille W, Bernklau D and Riechert H 1999 *Appl. Phys. Lett.* **75** 965
- [56] Neuberger R, Müller G, Ambacher O and Stutzmann M 2001 *Phys. Status Solidi* **RRN01** 6
- [57] Karrer U, Ambacher O and Stutzmann M 2000 *Appl. Phys. Lett.* **77** 2012
- [58] Ridley B K, Ambacher O and Eastman L F 2000 *Semicond. Sci. Technol.* **15** 270
- [59] Bernardini F and Fiorentini V 1997 *Phys. Rev. Lett.* **79** 3958
- [60] Yu L S, Qiao D J, Xing Q J, Lau S S, Boutros K S and Redwing J M 1998 *Appl. Phys. Lett.* **73** 238
- [61] Stepanov S, Wang W N, Yavich B S, Bougrov V, Rebane Y T and Shreter Y G 2001 *Mater. Res. Soc. Int. J. Nitr. Semicond. Res.* **6** 6
- [62] Lukitsch M J, Danylyuk Y V, Naik V M, Huang C, Auner G W, Rimai L and Naik R 2001 *Appl. Phys. Lett.* **79** 632
- [63] Brunner D, Angerer H, Bustarret E, Höppler R, Dimitrov R, Ambacher O and Stutzmann M 1997 *J. Appl. Phys.* **82** 5090
- [64] Martin G, Strite S, Botchkarev A, Agarwal A, Rockett A, Morkoc H, Lambrecht W R L and Segall B 1994 *Appl. Phys. Lett.* **65** 610
- [65] Martin G, Botchkarev A, Rockett A and Morkoc H 1996 *Appl. Phys. Lett.* **68** 2541
- [66] Wong L W, Cai S J, Li R, Wang K, Jiang H W and Chen M 1998 *Appl. Phys. Lett.* **73** 1391

-
- [67] Foutz B E, Murphy M J, Ambacher O, Tilak V, Smart J, Shealy J R, Schaff W J and Eastman L F 1999 *Mater. Res. Soc. Proc.* **572** 501
- [68] Smorchkova I P, Elsass C R, Ibbetson J P, Vetry R, Heying B, Fini P, Haus E, DenBaars S P, Speck J S and Mishra U K 1999 *J. Appl. Phys.* **86** 4520
- [69] Bougrioua Z, Farvacque J-L, Moerman I and Carosella F 2001 *Phys. Status Solidi* (b) at press
- [70] Asbeck P M, Yu E T, Lau S S, Sullivan G J, Van Hove J and Redwing J M 1997 *Electron Lett.* **33** 1230
- [71] Yu E T, Sullivan G J, Asbeck P M, Wang C D, Qiao D and Lau S S 1997 *Appl. Phys. Lett.* **71** 2794
- [72] Sala F D, di Carlo A, Lugli P, Bernardini F, Fiorentini V, Scholz R and Januc J-M 1999 *Appl. Phys. Lett.* **74** 2002
- [73] Eckey L, Hoffmann A, Thurian P, Broser I, Meyer B K and Hiramatsu K 1998 *Mater. Res. Soc. Symp. Proc.* **482** 555
- [74] Wetzel C, Takeuchi T, Amano H and Akasaki I 1999 *Japan. J. Appl. Phys.* **38** L163